

# UC Berkeley

## UC Berkeley Previously Published Works

### Title

Evaluation of accessible mineral surface areas for improved prediction of mineral reaction rates in porous media

### Permalink

<https://escholarship.org/uc/item/47r1w7cp>

### Authors

Beckingham, Lauren E  
Steeffel, Carl I  
Swift, Alexander M  
et al.

### Publication Date

2017-05-01

### DOI

10.1016/j.gca.2017.02.006

Peer reviewed

# Evaluation of accessible mineral surface areas for improved prediction of mineral reaction rates in porous media

Author links open overlay panel [Lauren E. Beckingham<sup>a,b</sup>](#) [Carl I. Steefel<sup>a</sup>](#) [Alexander M. Swift<sup>c</sup>](#) [Marco Voltolini<sup>a</sup>](#) [Li Yang<sup>a</sup>](#) [Lawrence M. Anovitz<sup>d</sup>](#) [Julia M. Sheets<sup>c</sup>](#) [David R. Cole<sup>c</sup>](#) [Timothy J. Kneafsey<sup>a</sup>](#) [Elizabeth H. Mitnick<sup>a</sup>](#) [Shuo Zhang<sup>c</sup>](#) [Gautier Landrot](#) [Jonathan B. Ajo-Franklin<sup>a</sup>](#) [Donald J. DePaolo<sup>a,e</sup>](#) [Saeko Mito<sup>a</sup>](#) [Ziqiu Xue<sup>a</sup>](#)  
Show more

<https://doi.org/10.1016/j.gca.2017.02.006> [Get rights and content](#)

## Abstract

The rates of mineral dissolution reactions in [porous media](#) are difficult to predict, in part because of a lack of understanding of mineral reactive surface area in natural porous media. Common estimates of mineral reactive surface area used in [reactive transport](#) models for porous media are typically ad hoc and often based on average [grain size](#), increased to account for [surface roughness](#) or decreased by several orders of magnitude to account for reduced surface reactivity of field as opposed to laboratory samples. In this study, accessible [mineral surface](#) areas are determined for a sample from the reservoir formation at the Nagaoka pilot CO<sub>2</sub> injection site (Japan) using a multi-scale image analysis based on [synchrotron X-ray](#) microCT, [SEM](#), [QEMSCAN](#), [XRD](#), [SANS](#), and [FIB-SEM](#). This analysis not only accounts for accessibility of mineral surfaces to [macro-pores](#), but also accessibility through connected micro-pores in [smectite](#), the most abundant [clay mineral](#) in this sample. While the imaging analysis reveals that most of the micro- and macro-pores are well connected, some [pore](#) regions are unconnected and thus inaccessible to [fluid flow](#) and diffusion. To evaluate whether mineral accessible surface area accurately reflects reactive surface area a flow-through core experiment is performed and modeled at the continuum scale. The core experiment is performed under conditions replicating the pilot site and the evolution of [effluent](#) solutes in the aqueous phase is tracked. Various reactive surface area models are evaluated for their ability to capture the observed effluent chemistry, beginning with parameter values determined as a best fit to a disaggregated sediment experiment (Beckingham et al., 2016) described previously. Simulations that assume that all mineral surfaces are accessible (as in the disaggregated sediment experiment) over-predict the observed mineral reaction rates, suggesting that a reduction of RSA by a factor of 10–20 is required to match the core flood experimental data. While the fit of the effluent chemistry (and inferred mineral dissolution rates) greatly improve when the pore-accessible mineral surface areas are

used, it was also necessary to include highly reactive glass phases to match the experimental observations, in agreement with conclusions from the disaggregated sediment experiment. It is hypothesized here that the 10–20 reduction in reactive surface areas based on the limited pore accessibility of reactive phases in core flood experiment may be reasonable for poorly sorted and cemented sediments like those at the Nagaoka site, although this reflects pore rather than larger scale heterogeneity.

## Keywords

Reactive surface area

Mineral accessibility

Mineral reaction rates

CO<sub>2</sub>sequestration

## 1. Introduction

The spatial and [temporal evolution](#) of a variety of geochemical systems can be simulated using [reactive transport](#) models, yet prediction of in-situ mineral reaction rates remains challenging. Modeled mineral reaction rates are often based on laboratory-determined rates; unfortunately, large discrepancies remain between observed field and laboratory rates, a mismatch which decreases the predictive value of such models when applied to new systems ([Brantley et al., 2008](#), [Pham et al., 2011](#), [Liu et al., 2012](#), [Liu et al., 2015](#)). While studies have suggested factors that contribute to these rate discrepancies (ie. the coupling of mineral dissolution and precipitation reactions [Maher et al., 2009](#), [Zhu and Lu, 2013](#)), there remains a lack of understanding and consensus on the controlling factors. Modeling studies struggle to not only simulate observed field rates, but also to accurately simulate laboratory reaction rates. Commonly, a reaction rate law is used where the mineral reaction rate is given by

$$(1a) R_m = A_m a_{H^+}^n k (1 - Q/K_m)$$

$$(1b) R_m = A_m a_{H^+}^n k [f \Delta G_r]$$

where  $A_m$  is the bulk reactive surface area (m<sup>2</sup> mineral/m<sup>3</sup> porous medium),  $k$  is the rate constant,  $a_{H^+}$  is the activity of  $H^+$ ,  $n$  is the pH dependence of the reaction,  $Q$  is the ion activity product, and  $K_m$  is the equilibrium constant ([Steefel and Lasaga, 1994](#), [Steefel et al., 2015a](#)). Rate law parameters are often arbitrarily adjusted so simulated rates match observed dissolution rates, as summarized by the review in [Gaus et al. \(2008\)](#). One of the most commonly, and arbitrarily, adjusted parameters in continuum scale modeling is mineral reactive surface area (RSA).

Currently there is no protocol for determining mineral reactive surface areas and they are often estimated using one of many specific surface area (SSA) or effective surface area (ESA) approximations ([Brantley et al., 2008](#), [Bourg et al., 2015](#), [Beckingham et al., 2016](#)). SSA approximations include geometric surface areas calculated assuming geometry and average grain diameter, image perimeter based surface area, and laboratory measured BET surface area as summarized in [Beckingham et al. \(2016\)](#). Effective surface areas are those that account for the distribution of reactive sites on [mineral surfaces](#), [surface roughness](#), or mineral accessibility, for example ([Beckingham et al., 2016](#)). These are typically calculated by applying a scaling factor (SF) to a specific surface area ([Beckingham et al., 2016](#)). This range of approaches to surface area estimation results in multiple orders of magnitude variation in RSA values ([Bourg et al., 2015](#), [Beckingham et al., 2016](#)). In reactive transport simulations, variations in mineral reactive surfaces areas result not only in discrepancies in mineral reaction rates, but [porosity](#) and reactive plume evolution as well ([Gaus et al., 2008](#), [Atchley et al., 2014](#)).

Despite the range of methods used to estimate reactive surface area, “porous medium effects” (e.g. [pore scale](#) transport limitations) on the surface area of reactive minerals are often not accounted for in simulations of field systems. Laboratory mineral dissolution experiments typically are based on well-mixed powder dissolution experiments where geometric surface area estimates, or some variation of a geometric approach as described above, reflect an actual physical approximation of the reacting mineral surfaces. An experimental and modeling study of [weathering rates](#) in soil in [Parry et al. \(2015\)](#) found dissolution rates normalized to geometric surface areas to be greater than those normalized to BET surface areas and that regardless of which surface area estimate was used, laboratory rates were higher than observed field dissolution rates. This may be because these surface area estimates do not accurately reflect the surface area available for reaction in porous media. In contrast with idealized laboratory studies, field systems rarely have uniformly sized particles, may have variations in liquid saturation (water content), or mineral surfaces may be inaccessible due to disconnected pores, [cementation](#) or clay coatings (e.g. [Ganor et al., 2005](#), [Béarat et al., 2006](#), [Peters, 2009](#), [Crandell et al., 2012](#), [Landrot et al., 2012](#), [Nishiyama and Yokoyama, 2013](#), [Waldmann et al., 2014](#)). In these systems, therefore, mineral abundance alone may not accurately reflect the accessibility of mineral surfaces to reactive fluids and the effect of transport limitations needs to be considered ([Brantley et al., 2008](#), [Scislewski and Zuddas, 2010](#), [Salehikhoo and Li, 2015](#)). In addition, existing estimates of reactive surface area do not account for the possibility that reactive surface

area may evolve during reaction due to dissolution or armoring ([Luquot and Gouze, 2009](#), [Noiriel et al., 2009](#), [Scislewski and Zuddas, 2010](#), [Gouze and Luquot, 2011](#)). Recent laboratory and modeling studies have revealed the importance of accounting for spatial heterogeneity in surface areas and reactive mineral-fluid interfaces in reactive transport simulations. [Atchley et al. \(2014\)](#) found heterogeneity in the [spatial distribution](#) of reactive surface area resulted in variations in the simulated spatial and temporal plume evolution, transport time, and reactive length scales. [Salehikhoo and Li \(2015\)](#) were able to successfully simulate experimentally observed dissolution rates in a heterogeneous column experiment by accounting for the reactive mineral-fluid interface. Accounting for the mineral-fluid surface also enabled successful simulation of laboratory reaction rates in an unsaturated system in [Nishiyama and Yokoyama \(2013\)](#) where water films on mineral surfaces maintained mineral dissolution reactions in the presence of air.

However, determining the accessible surface area in real [porous materials](#) is challenging. Recent studies have made efforts to obtain estimates of accessible reactive surface area. In [sandstone](#) samples, 2D [scanning electron microscopy](#) (SEM) backscattered electron (BSE) imaging has revealed clay coatings on grain surfaces that limited accessibility to other mineral surfaces ([Peters, 2009](#), [Waldmann et al., 2014](#), [Lai et al., 2015](#)). [Waldmann et al. \(2014\)](#) determined minerals at the pore-mineral interface using 2D [SEM BSE](#) images. [Landrot et al. \(2012\)](#) combined 2D SEM BSE and energy dispersive [spectroscopy](#) (EDS) imaging with focused [ion-beam](#) (FIB) SEM and [X-ray](#) micro computed [tomography](#) (CT) to examine mineral accessibility and connected porosity in samples from the Cranfield CO<sub>2</sub> storage site. In their sample, connected porosity and access to mineral surfaces were drastically underestimated when connected micro-pores in [chlorite](#) were neglected ([Landrot et al., 2012](#)).

In this work, a multi-scale 2D and 3D imaging analysis method is used to examine the accessible mineral surface areas of a [reservoir rock](#) sample from the Nagaoka pilot CO<sub>2</sub> injection site in Japan. This includes identification of the connected micro- and macro-scale porosity and associated accessible mineral surfaces. 2D SEM and 3D X-ray CT imaging is used at the [macropore](#) scale coupled with FIB-SEM and (ultra-) small angle [neutron scattering](#) (USANS/SANS) at the nano-scale. A laboratory core flow-through experiment is performed on the same sample as was used in the 3D X-ray CT imaging and the evolution of [effluents](#) tracked. Reactive transport modeling of the core experiment was used to evaluate specific and accessible surface area estimates that provide the best fit of the effluent chemistry, allowing us to compare reactivity under differing flow and porosity conditions from the previous disaggregated sediment

experiment ([Beckingham et al., 2016](#)). By comparing the disaggregated sediment experiment ([Beckingham et al., 2016](#)) and the core flood experiment described here, we attempt to quantify the “porous medium” effects on subsurface reaction rates. Although we focus on the CO<sub>2</sub>/brine/mineral systems relevant to geological [carbon storage](#), the fundamental problem of surface area estimation for mineral reaction rates has broad implications for the interpretation of subsurface [geochemistry](#).

## 2. Materials and methods

### 2.1. Sample

Samples from the reservoir formation at the Nagaoka CO<sub>2</sub> pilot injection site in Nagaoka, Japan were used in this study. At this site, the Pleistocene Haizume formation is the target formation for CO<sub>2</sub> injection ([Mito et al., 2008](#)). This formation is a volcanogenic [sandstone](#) with interbedded layers of [siltstone](#) and [mudstone](#) ([Chiyonobu et al., 2013](#)). Subsamples from cores extracted from a depth of 1093 m before CO<sub>2</sub> injection began were used here and in the previous study in [Beckingham et al. \(2016\)](#). The composition of the [reservoir rock](#) was determined using X-ray Fluorescence (XRF), X-ray Diffraction (XRD), and 2D [SEM](#) Quantitative Evaluation of Minerals by [SCANning electron microscopy](#) (QEMSCAN®) as detailed in [Beckingham et al. \(2016\)](#). These analyses found the samples to be predominantly [quartz](#) (27.6 vol. %), [plagioclase feldspar](#) (22.6 vol.%), [smectite](#) (17 vol.%), K-feldspar (13.4 vol.%) and [pyroxene](#) (7.2 vol.%). The detailed composition, including minor mineral phases is given in [Table 1](#). XRD analysis carried out in [Beckingham et al. \(2016\)](#) also found the sample to consist of 8.5 wt.% [amorphous material](#) consisting of glass and clays.

Table 1. Mineral abundances and accessibilities as determined from pixel analysis in the 2D registered [BSE](#) and QEMSCAN image where mineral abundance (A) is the distribution of minerals by volume%. The accessibility of minerals is evaluated by considering minerals adjacent to all [pores](#) identified in the 2D BSE images (column B) and minerals adjacent to connected (macro and meso) pores (column C).

Mineral	A. Abundance (%)	B. Accessible % (all BSE pores)	C. Acc (conne and m
Quartz	27.64	20.16	1:
Plagioclase	21.4	19.48	14
Albite	6.46		
An25	1.49		
Labradorite	13.46		
Smectite	16.99	32.43	30
K-feldspar	14.62	8.06	6
Pyroxene	7.21	7.22	1
Fe,Mg rich	5.46		
Ca,Mg rich	1.72		
AlSitrap	2.74	1.63	3
Biotite	2.58	2.57	5
Amphibole	1.85	1.46	1
Others	1.41	2.44	2
Fe Hydroxide	1.22	1.07	0
Chlorite	1.17	1.34	1
Kaolinite	0.41	1.08	1
Pyrite	0.36	0.41	0
Serpentine	0.29	0.52	0
Ca-phosphate	0.07	0.08	0
Calcite	0.03	0.06	0

## 2.2. Multi-scale imaging and analysis

A multi-scale 2D (2.2.1) and 3D (2.2.4) imaging study, including nano-scale analysis of smectite [porosity](#) (2.2.2) and multi-scale (U)SANS analysis of porosity (2.2.3), was carried out to examine mineral accessible surface areas of unreacted samples.

### 2.2.1. 2D SEM image analysis

2D SEM [BSE](#) and QEMSCAN images (FEI Quanta 250 SEM) of a polished thin section were collected in [Beckingham et al. \(2016\)](#) and further analyzed here. In our previous work, a 16.9 mm<sup>2</sup> 2D SEM BSE image of a polished thin section was captured at a resolution of 0.2  $\mu$ m. The distribution of minerals was then determined through QEMSCAN analysis on the same sample area at a resolution of 2.5  $\mu$ m. Using image registration, mineralogical information was added to the high-resolution BSE images ([Beckingham et al., 2016](#)). Mineral abundances were then calculated by counting the

number of pixels of each mineral in the 2D image. Image segmentation, to separate pore and grain pixels, was also performed and the porosity computed as 14.7%. In this study, the registered 2D image was used to determine accessible [mineral surfaces](#), or mineral surfaces at the pore-mineral interface. Using codes written in Matlab (MathWorks), the pore-mineral interfacial pixels were first identified. Mineral accessibilities were then computed for each mineral by counting the number of pixels of each mineral at the pore-mineral interface and dividing by the total number of interfacial pixels. This analysis considered mineral pixels adjacent to pores identified in the 0.2  $\mu\text{m}$  resolution segmented BSE image ([Beckingham et al., 2016](#)) and will be referred to as minerals accessible to “all BSE pores”.

Pore connectivity has been shown to significantly alter mineral accessibility in some systems ([Landrot et al., 2012](#)). Initial SEM imaging of the Nagaoka reservoir rock in [Beckingham et al. \(2016\)](#) revealed this sample has abundant smectite (17% by volume) present as a cement and grain coating. This suggests that estimates of the overall pore connectivity need to consider not only the connectivity of the BSE identified [macro-pores](#), but the connectivity of smectite micro-pores as well ([Steefel et al., 2015b](#)). Therefore, characterization of smectite micro-pores is investigated prior to determining the overall pore connectivity and accessible mineral surface areas. The nanoscale analysis of smectite using FIB-SEM and SANS is described in the following section.

#### 2.2.2. Nano-scale analysis of smectite

Smectite micro-pores were analyzed using high-resolution FIB-SEM imaging and SANS/USANS. FIB-SEM images were collected using a Zeiss XB1540 EsB at the Molecular [Foundry](#) at Lawrence Berkeley National Laboratory. The instrument has a GEMINI [field emission](#) column (FESEM) and an Orsay Physics focused [ion beam](#) and has a maximum resolution of 1.1 nm at 20 kV and 2.5 nm at 1 kV. The FIB column uses a liquid [gallium](#) source and has a resolution of 7–5 nm at 30 kV. Sample manipulation is performed on a 6-axis fully eucentric motorized stage.

A smectite-rich area in the thin section was identified in secondary electron mode based on texture and location as initially identified in the 2D QEMSCAN® images. A trench was milled with the FIB in front of the area of interest using a 10 nA probe current. Thirty-six sequential slices were then milled and imaged with a FIB current of 2 nA at a 75 nm spacing, and SEM resolution of 4.85 nm for each milled slice.

The 36 FIB-SEM images were cropped to an area of 10.85  $\mu\text{m} \times 11.09 \mu\text{m}$ , thus removing edge features that would make segmentation difficult. This corresponded to a total volume of  $3.246 \times 10^{-16} \text{ m}^3$ . Before segmentation, the local [image contrast](#) was enhanced and streak artifacts removed using the Enhance Local Contrast, [FFT](#) and Inverse FFT plug-ins in ImageJ ([Rasband, 1997](#)). To further improve contrast between the pore and grain pixels, images were processed using a bilateral filter before segmentation. Pore and grain pixels were segmented following the optimization method developed in [Peters \(2009\)](#) that determines the [inflection point](#) of overlapping intensity distributions while minimizing errors in misclassified pixels. This is the same procedure that was used to calculate the pore-grain threshold for the BSE images in the initial study in Beckingham et al. 2015. Given variations in individual image brightness and contrast, the threshold for each 2D image was determined independently. Following segmentation, the total porosity and slice porosities were calculated by first counting the number of pore pixels in each image and then dividing by the respective total number of pixels.

The connected smectite porosity was then determined from the segmented volume using a [burning](#) algorithm, following the approach of [Landrot et al. \(2012\)](#). Pores on the face of the cuboid were first identified followed by connected pores in the adjacent layer. This procedure considered pores starting on each face of the cuboid and was iterated until the entire volume was analyzed. The corresponding connected surface area was computed in Matlab via a “marching cubes” algorithm ([Landrot et al., 2012](#)). This algorithm used the isosurface function of Matlab to draw patches within the connected pore network. Patch surface areas were then calculated and summed.

### 2.2.3. SANS/USANS

A combination of small- and ultra small-angle [neutron scattering](#) experiments (SANS, USANS) were performed on thick sections of these samples ([Beckingham et al., 2016](#)) to quantify total porosity, pore size distribution, and total surface area. [Neutrons](#) penetrate earth materials far more readily than do [X-rays](#), making it possible to interrogate relatively large volumes of rock ( $>30 \text{ mm}^3$ ) with statistically meaningful numbers of pores for much of the size range found in the Nagaoka samples. The signal detected by SANS and USANS arises primarily from the squared difference in scattering length density (SLD) between interfaces, including mineral-pore and mineral–mineral contacts. The SLD of a material  $j$  is given by:

$$(2) \rho_j^* = \sum_{i=1}^n b_{ij} N_{AMi}$$

where  $b_i$  is the bound coherent scattering length of atom  $i$ ,  $N$  the total number of atoms in the molecule,  $\rho_i$  is the mass density,  $N_A$  is the Avogadro constant and  $M_i$  is the molar mass. For most minerals, the  $\Delta$ SLD between mineral–mineral contacts is sufficiently low compared to the  $\Delta$ SLD between mineral and pores that a two-phase approximation can be applied to the data and only mineral-pore contacts need be considered ([Anovitz and Cole, 2015](#)).

SANS measurements were performed on the GP-SANS instrument at the High Flux Isotope Reactor (HFIR), Oak Ridge National Laboratory ([Littrell et al., 2008](#)) Two series of measurements were taken. The first used a detector distance of 1.5 m, a wavelength  $\lambda = 4.75 \text{ \AA}$ , and a wavelength spread  $\Delta\lambda/\lambda = 0.14$ ; the second used a detector distance of 20 m, a wavelength  $\lambda = 19 \text{ \AA}$ , and a wavelength spread  $\Delta\lambda/\lambda = 0.14$ . The resultant scattering vector  $Q$  ranged from  $5 \times 10^{-4}$  to  $0.3 \text{ \AA}^{-1}$ . USANS measurements were performed on the BT5 instrument at the Center for Neutron Research at the National Institute of Standards and Technology ([Barker et al., 2005](#)), with wavelength =  $8.09 \text{ \AA}$  and wavelength spread  $\Delta\lambda/\lambda = 0.11$ , and  $Q$  vectors ranging from  $2.8 \times 10^{-5}$  to  $2.5 \times 10^{-3} \text{ \AA}^{-1}$ . As the scattering vector  $Q$  increases, the size of the objects that contribute to the scattering signal decreases, according to Bragg's law:  $|Q| = 2\pi/d = 4\pi \sin\theta/\lambda$ , where  $d$  is the distance between scattering surfaces,  $\theta$  is the scattering angle, and  $\lambda$  is the neutron wavelength. The scale of objects investigated by the combination of neutron scattering methods therefore ranges from  $\sim 1 \text{ nm}$  to  $\sim 25 \text{ microns}$ . Both scattering experiments used polished rock sections approximately 150 microns thick and [cadmium](#) masks to define the rock volume to be investigated. Backscattered electron images of the [pore space](#) were used to extend the scattering curve to larger scales. Additional details of the data reduction procedures for both neutron scattering and the use of imagery may be found in ([Anovitz et al., 2009](#), [Anovitz et al., 2013](#), [Anovitz and Cole, 2015](#), [Wang et al., 2013](#)).

Modeling of the reduced data to yield total porosity, pore size distribution, and total surface area requires several additional parameters to be calculated. For the two-phase approximation used here, the average coherent scattering length density (SLD) of a multi-mineralic rock can be calculated as ([Radlinski et al., 1996](#)):

$$(3) \rho_{\text{prock}} = N_A d M \sum_j \rho_j \sum_i b_i$$

where  $N_A$  is Avogadro's number,  $M$  is the average formula weight in a given mass of the rock (number of formula units of each mineral, times their formula weight, divided by the total number of formula units) and  $d$  is the physical density (volume average) of the rock as a whole. For these samples, the matrix (rock) density is  $2.70 \text{ g/cm}^3$  and the SLD is

3.92E-6. By contrast, the coherent SLD of the epoxy used was determined by testing to be effectively zero.

Total porosity is obtained from the scattering curves using the invariant  $Y$ , calculated as:

$$(4) Y = \int_0^\infty Q^2 I(Q) dQ = 2\pi^2 (\Delta\rho)^2 \phi (1-\phi)$$

where  $\Delta\rho$  is the difference in scattering length density between rock and pores, and  $\phi$  is the porosity. Within a sufficiently large range of integration, each scattering data point can be used to determine the increase in porosity contributed by scattering objects averaging a scale of  $2\pi/Q$ .

Total surface area is commonly calculated from the pore size distribution of total porosity using a geometric model of pore shape. In most studies, pores are assumed to be non-uniform spheres, an approach that can yield valid results for pores

within [granular material](#) or in [limestone](#). For geological materials with abundant clays, such as the Nagaoka, this approximation is less valid. Clays, including smectite, host pores shaped like slits or wedges. Scattering objects in the Nagaoka samples are therefore modeled using a dual-geometry approach: spherical pores for objects

sufficiently larger than the pores observed in smectite, slit-shaped pores for objects sufficiently smaller than such sizes, and a mix of the two if nearly equal. Given an increase in specific pore volume ( $\Delta SV_{\text{pore},d}$ ), in units of volume per unit mass, for scattering objects of a scale  $d$ , the volume of each object is

either  $V_{\text{sphere}} = 1/3\pi d^3$  or  $V_{\text{slit}} = \pi d r_{\text{slit}}$ , where  $r_{\text{slit}}$  is the average radius of intact

smectite [platelets](#). This has been previously determined to be roughly 0.125 microns by observation of smectite-rich materials ([Nadeau et al., 1985](#)); this value is at least approximately consistent with findings of SEM examination of the smectite in the

Nagaoka samples. Given pore and scattering object volumes, the number of pores,  $\text{Num}_{\text{pores}}$ , of both slit and spherical geometries in each gram of sample is calculated as:

$$(5) \text{Num}_{\text{pores}} = \text{Frac}_{\text{slit}} * \Delta SV_{\text{pore},d} / V_{\text{slit}} + (1 - \text{Frac}_{\text{slit}}) * \Delta SV_{\text{pore},d} / V_{\text{sphere}}$$

where  $\text{Frac}_{\text{slit}}$  is 0 for scattering objects at least one order of magnitude larger than  $r_{\text{slit}}$ , 1 for objects at least one order of magnitude smaller than  $r_{\text{slit}}$ , and otherwise calculated from the volume proportions of each shape, expressed in terms of  $V_{\text{Frac}_{\text{slit}}}$ , as:

$$(6) V_{\text{Frac}_{\text{slit}}} = 0.5 + \log_{10} r_{\text{slit}} - \log_{10} d$$

and

$$(7) \text{Frac}_{\text{slit}} = (V_{\text{Frac}_{\text{slit}}} * V_{\text{slit}}) / (V_{\text{Frac}_{\text{slit}}} * V_{\text{slit}} + (1 - V_{\text{Frac}_{\text{slit}}}) * V_{\text{sphere}})$$

Given a number of pores, and a calculation of the fraction of slits and spheres, the specific surface area (SSA) is given as:

$$(8) \text{SSA} = \Delta SV_{\text{pore},d} * \text{Frac}_{\text{slit}} * (2 * \pi r_{\text{slit}}) + (1 - \text{Frac}_{\text{slit}}) * (\pi d)$$

## 2.2.4. 3D Imaging and analyses

### 2.2.4.1. Synchrotron X-ray $\mu$ CT

[Synchrotron](#) X-ray micro Computed [Tomography](#) (X-ray  $\mu$ CT) was used to obtain digital 3D volumes of selected tiles of the sample. The measurements were carried out at the Advanced Light Source at the Lawrence Berkeley National Laboratory. Beamline 8.3.2, a hard XR imaging beamline ([MacDowell et al., 2012](#)), was chosen for the measurement. The sample, mounted on a wooden stub, was measured in a “local area” configuration -the sample was slightly larger than the [field of view](#) (FOV  $\sim 0.83$  mm), using a continuous tomography procedure. The experiment was conducted using a multilayer [monochromator](#) and a 20 keV XR beam. The optical chain included a 11  $\mu$ m thin Eu-doped GGG [scintillator](#), a 20 $\times$  magnification Mitutoyo objective lens in a Optique Peter (Optique Peter, Lyon, France) microscope, and a PCO Edge sCMOS camera (PCO AG, Kelheim, Germany) for collecting the images. Exposure time was 1.5 s and the total number of projections collected was 2049. The pixel size was 325 nm, in a FOV of 2560 px  $\times$  2160 px, and the actual resolution on a single projection, checked with a nanofabricated pattern (XRadia Inc.), was sub-micron.

The reconstruction of the 3D volume was carried out first using a single-distance phase retrieval algorithm on the projections (after flat- and dark- field corrections), using the [Paganin et al. \(2002\)](#) algorithm implemented in the ANKAphase software ([Weitkamp et al., 2011](#)). This procedure can be applied to data collected in the near-field region (in our measurement the sample-to-detector distance was  $\sim 5$  mm) using spatially coherent XR, such as the ones from synchrotron light sources. The advantage of phase retrieval in this case included better contrast between the different phases and reduction of [phase contrast](#) effects at the borders of objects, thus aiding both visualization and quantitative segmentation procedures. Once the new projections were calculated, a conventional reconstruction procedure was followed, including normalization, noise filtering, sinogram generation, and inversion using a filtered back projection algorithm to calculate the single horizontal “slices”, the components of the final 3D volume. This last part of this sequence was carried out with the commercial software [Octopus](#) ([Dierick et al., 2004](#)).

### 2.2.4.2. 3D Image segmentation

Image artifacts precluded use of a simple thresholding procedure and required pre-processing using a modified mask to remove noise and preserve [grain boundaries](#). First, the CT images were thresholded in ImageJ with a manually selected threshold.

This threshold was selected to provide the best representation of the grain structures, although the results contained significant noise in the pore space. These misidentified grain pixels were removed using the “remove outliers” function in ImageJ with a radius of 3, significantly smaller than the typical pore size. A mask was then created by thresholding a copy of the original CT images with a different, manually selected, threshold that provided a better depiction of the pore space. Noise pixels in the mask image were then also removed using the *Remove Outliers* function in ImageJ. Due to image artifacts, some manual processing of grain and pore pixels was required. The mask image was then dilated to ensure the grain morphology would be preserved when applying the mask to the segmented image. Using image calculator with the “AND” function in ImageJ, the mask was then applied to the segmented image to produce the final segmented image.

The analyses described in previous sections reflect only the pore connectivity in 2D. To account for the 3D connectivity of the reservoir rock, the connectivity and corresponding connected surface areas in 3D were calculated from the micro-CT images. To account for the 3D connectivity corresponding to the 2D area analyzed, 3D cuboids with the same total 2D slice area as the 2D registered image, 16.9 mm<sup>2</sup>, were randomly sampled from the larger 3D image. This corresponded to a cuboid volume of 0.052 mm<sup>3</sup>. Ten randomly sampled cuboids were selected from the binary CT images and the connected 3D pore space was identified using the Find Connected Regions plugin for ImageJ. The mineral surface area in contact with the connected pore network was then calculated using a marching cubes algorithm, as described for analysis of the smectite surface area in Section [2.2.4](#).

### 2.3. Core flood experiment

A core flood experiment was conducted to investigate the [cation](#) release behavior from Nagaoka [sediment core](#) samples during invasion by CO<sub>2</sub>-saturated brine and the relationship with corresponding sediment pore structures and actual accessible reactive mineral surface areas. The experiment was performed on a custom-built miniature triaxial core holder capable of providing axial and [confining pressures](#) up to 3500 psi and temperature up to 75 °C. A core sample (5 mm O.D and 16 mm length) cored out of undisturbed Nagaoka sediments was jacketed using PTFE heat shrink tube and loaded into the high pressure experiment cell. Axial and confining pressure was provided by a high-pressure syringe pump (ISCO 65 DM) under constant pressure mode at ~110 bar. A second syringe pump was used to inject the CO<sub>2</sub>-containing saline water (0.1 M NaCl) into the core sample under constant flow mode (~0.4 μL/min). The [pore pressure](#) was

maintained at ~100 bar by a back-pressure regulator at the end of the outlet line after flowing through a 0.5 micron inline filter. The experimental cell was mounted on a thermostatic hot plate, covered with an aluminum cylinder shield and monitored with a [temperature probe](#) to keep the experiment system at 50 °C constant temperature. [Effluent](#) solution samples were collected every 24 h and analyzed using an ICP-MS (Perkin Elmer Elan DRCII) to monitor the evolution of the [solution chemistry](#).

## 2.4. Reactive transport modeling of core flood experiment

### 2.4.1. Model description

Continuum [reactive transport](#) simulations of the core experiment were carried out using CrunchFlow ([Steeffel et al., 2015a](#)) in 1-D using the dimensions of the column and assuming an initially homogeneous distribution of mineral [volume fractions](#) and a porosity of 21.8%. The total length of the column was 1.6 cm and this was discretized with 100 grid cells of 0.16 mm. The Darcy flux calculated by dividing the volumetric flow rate by the cross sectional area of the column was  $2.04 \times 10^{-5} \text{ m}^3/\text{m}^2/\text{min}$ .

The governing equation solved is given by ([Steeffel et al., 2015a](#)):

$$\partial(\phi\Psi_i)/\partial t = \nabla \cdot (\phi D_i \nabla \Psi_i) - \nabla \cdot (q\Psi_i) - \sum_{m=1}^N v_{im} R_m$$

where  $\Psi$  is the total concentration,  $\phi$  is the porosity,  $D^*$  is the dispersion coefficient (combining [hydrodynamic](#) dispersion and molecular diffusion), and  $q$  is the Darcy flux,  $v_m$  are the stoichiometric coefficients for the mineral dissolution reactions, and  $R_m$  are the rates.

Simulations were carried out using accessible and specific mineral surface areas as discussed below (Section [2.4.2](#)), and compared with effluent experimental [ion concentrations](#). Mineral dissolution rate constants that account for the pH and temperature dependencies of reaction rates were used in the simulations and are given in [Appendix A](#). The pH dependencies used in the simulations ([Appendix A](#)) were such that they reproduce the single value rate constants at pH 3.2 used in the disaggregated powder experiment simulations. An explicit pH dependence was necessary because the simulations (discussed below) suggest an increase of 0.48 pH units over the length of the 16 mm column. Both mineral dissolution and precipitation were considered, although in general the low pH of the solution prevented [supersaturation](#) of any common possible secondary phases. In addition, cation exchange was considered by introducing a bulk [cation exchange capacity](#) of 120 micro-equivalents per gram sediment, a reasonable value for a sediment containing moderate amounts of clay ([Steeffel et al., 2003](#)).

#### 2.4.2. Mineral surface area evaluation

Mineral specific and effective surface areas of the Nagaoka reservoir rock were evaluated in [Beckingham et al. \(2016\)](#). This included specific surface area estimates from existing literature studies that measured the BET surface area of pure minerals in addition to a new image perimeter approach that quantified surface areas in the 2D SEM image. Effective surface areas included a scaled geometric approach that was used in prior modeling of the Nagaoka site ([Mito et al., 2013](#)) and a one order of magnitude scaling factor applied to the image perimeter specific surface areas. These specific and effective surface areas were evaluated through continuum scale modeling of a disaggregated mineral dissolution experiment. The disaggregated experiment was run under the same experimental temperature and pressure conditions as in this study and the disaggregated sample and sub-core in this study were obtained from the same core. Simulation results indicated that inclusion of [grain size](#) distributions and size-dependent specific surface areas for plagioclase and pyroxene minerals were needed to account for the observed early time experimental behavior. In addition, high Ca and Mg to Si ratios indicated cation leaching or dissolution of a highly reactive glass phase that contributed significantly to the initial concentration peaks. The presence of the glass phase was also evident in the XRD analysis and SEM imaging ([Beckingham et al., 2016](#)). With the inclusion of the grain size distributions and glass phase, the simulations that provided the best fit with the experimental observations used the image perimeter based specific surface areas ([Beckingham et al., 2016](#)).

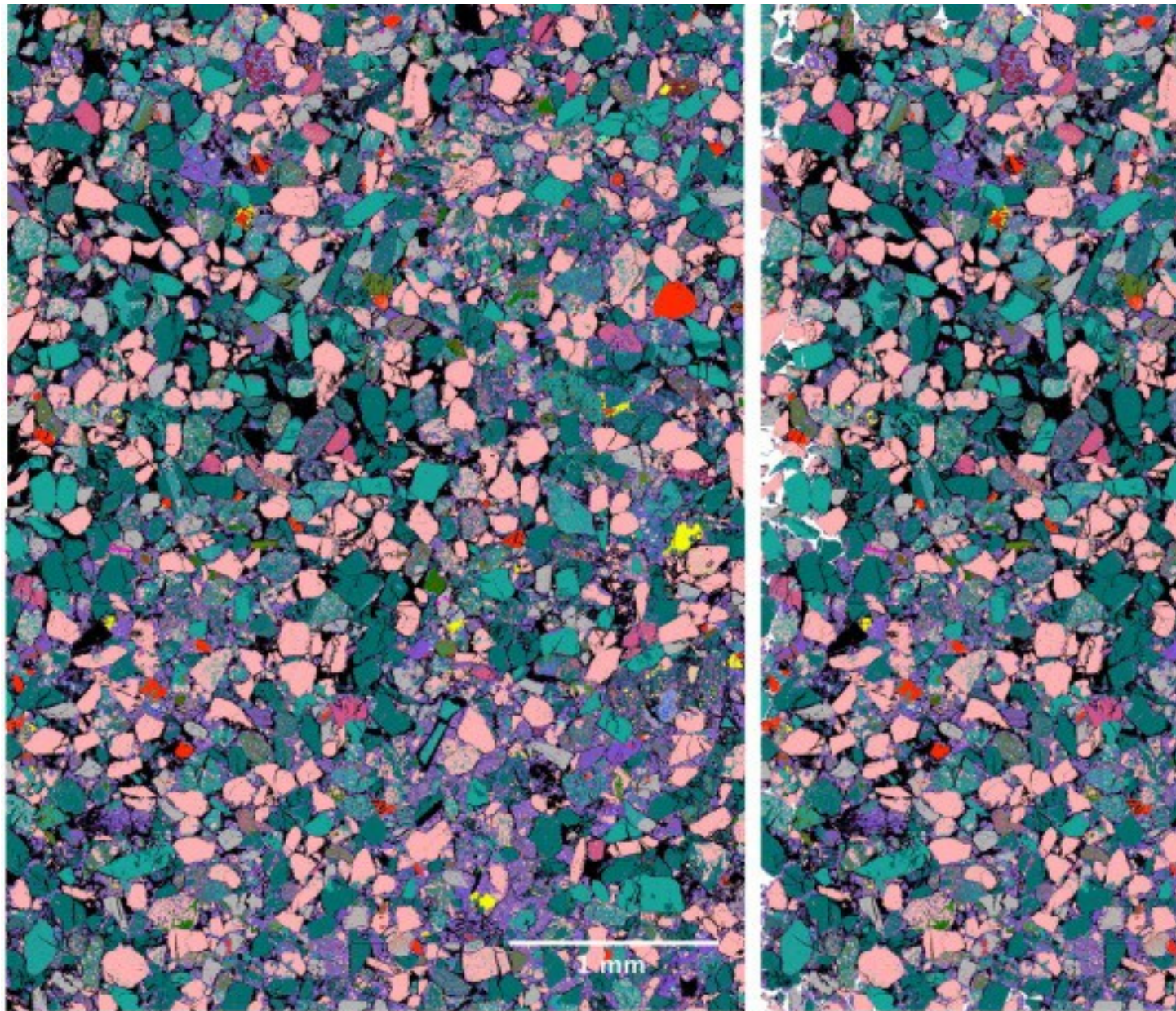
In this study, two estimates of mineral reactive surface areas will be evaluated. First, the surface areas that provided the best-fit simulation in the disaggregated Nagaoka sediment study ([Beckingham et al., 2016](#)) will be used in the reactive transport simulations to compare against observed effluent concentrations of total  $\text{Ca}^{2+}$ ,  $\text{Mg}^{2+}$ , and dissolved  $\text{SiO}_2$ . Second, the multi-scale image obtained accessible surface areas from this study (Section [2.2](#)) will be tested against the data. The comparison of the best-fit surface area values from the disaggregated sediment experiment described in [Beckingham et al. \(2016\)](#) with the pore-accessible mineral surface areas determined in this study will provide guidance as to whether accessibility needs to be included in [field scale](#) simulations of water–rock reaction rates. Note that the pore accessibility adjustments to the RSA factor in pore (grain) scale heterogeneity and pore structure, but do not capture any further adjustments required at larger (>cm) length scales.

### 3. Results

#### 3.1. Multi-scale imaging of mineral accessibility

### 3.1.1. 2D SEM imaging

The registered 2D [SEM](#) QEMSCAN image of the Nagaoka sediment starting material is shown in [Fig. 1](#). In this image, each color corresponds to a different mineral as described in [Beckingham et al. \(2016\)](#). This sample contains an amorphous component consisting of glass and clays. The glass phase, however, was unable to be discretized in the QEMSCAN analysis and likely some of the pixels classified as AlSiTrap, Others, and a fraction of the [Smectite](#) pixels correspond instead to the glass phase ([Beckingham et al., 2016](#)). Accessible [mineral surfaces](#), defined as pixels of that mineral adjacent to the [BSE](#) segmented [pore](#) pixels, were calculated as described above (Section [2.2.1](#)) and the corresponding mineral accessibilities are given in [Table 1](#) (column B). These values reflect the percentage of the pore-mineral interface that corresponds to a specific mineral. For example, of the total pore-mineral interface pixels, 20.16% are [quartz](#) pixels. For most of the minerals, the abundance is greater than the corresponding accessibility. In other words, mineral abundance overestimates mineral accessibility. For [clay minerals](#), however, mineral abundance underestimates mineral accessibility. This is expected given that clay minerals often occur as a grain coatings (e.g. [Peters, 2009](#)). Smectite has the largest discrepancy between the two with an abundance of 17% and accessibility of 32%.



Quartz	Pyroxene	Others	Pyrite
Plagioclase	AlSilicate trap	Fe hydroxides	Serpentine
Low BSE	Biotite	Chlorite	Ca-phosphate
Smectite	Amphibole	'Kaolinite'	Calcite
K-Feldspar			

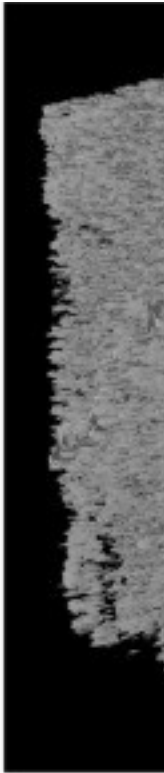
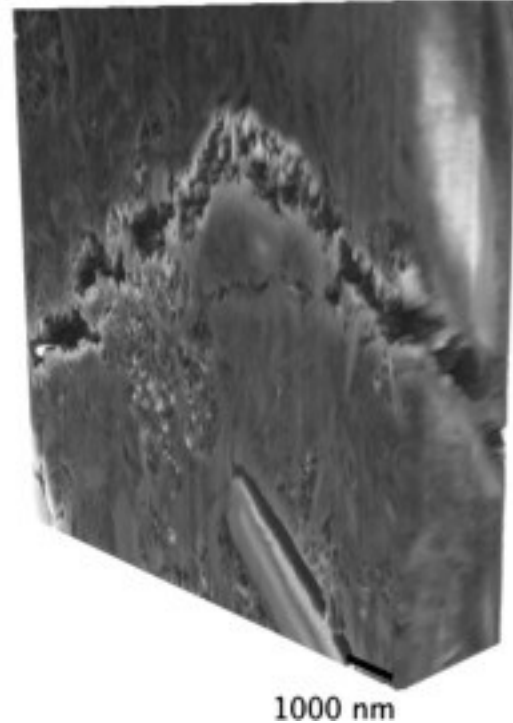
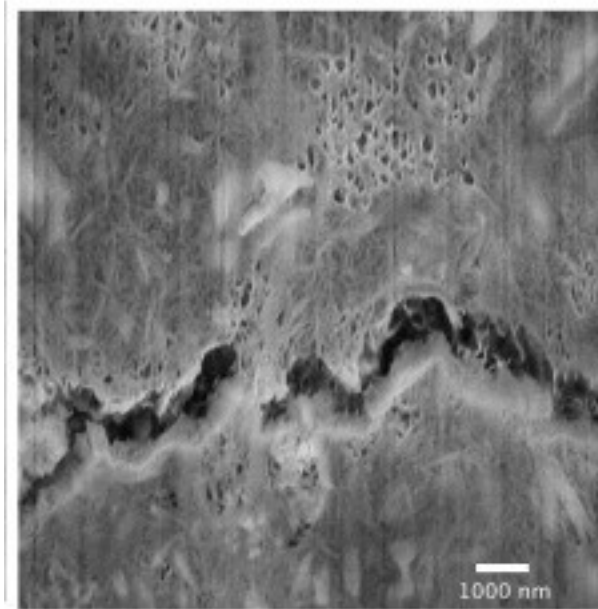
1. [Download high-res image \(1MB\)](#)
2. [Download full-size image](#)

Fig. 1. Registered [SEM BSE](#) and QEMSCAN image (left), and registered SEM BSE and QEMSCAN image with [macropore](#) connectivity analysis (right, white regions). The mineral distribution, as determined via the QEMSCAN analyses, is depicted by showing each mineral as a different color with [pores](#), labeled 'Low BSE', shown in black. The connectivity of the macro pore space is shown by depicting connected macro pores in

white and unconnected pores in black (right). (For interpretation of the references to color in this figure legend, the reader is referred to the web version of this article.)

### 3.1.2. FIB-SEM nano-scale analysis of smectite

A series of 2D FIB-SEM images that examine the smectitic portion of the unreacted Nagaoka sample were compiled to a 3D volume, as shown in [Fig. 2](#). The porosity was calculated to be 9.25% by counting pore pixels in the thresholded 3D volume. Of this total porosity, 51% is connected as determined by the [burning](#) algorithm described previously (Section [2.2.2](#)). The corresponding surface area of the connected [pore space](#), calculated from the marching cubes algorithm, is  $8.6 \times 10^{-9} \text{ m}^2$ . Given the total smectite volume analyzed by FIB-SEM of  $3.2 \times 10^{-16} \text{ m}^3$ , and assuming an average density of  $2.7 \text{ g/cm}^3$ , this corresponds to  $9.9 \text{ m}^2/\text{g}$ . As this accounts for 51% of the total smectite surface area, this agrees relatively well with the range of previously reported total smectite surface areas of  $34 \text{ m}^2/\text{g}$  to  $747 \text{ m}^2/\text{g}$  ([Metz et al., 2005](#)). It should be noted that the segmented FIB-SEM images likely underestimate the total porosity, as only pores with intensities significantly below those of the smectite mineral are quantified. This provides a conservative estimate of total and connected porosity ([Landrot et al., 2012](#)). Additionally, the 75 nm spacing between slices makes it possible to capture only some of the smaller pores that connect slices, thus contributing an additional underestimation of the surface area and porosity. It is assumed therefore that there is significant connected [micro-porosity](#) in the smectite regions such that access to underlying mineral surfaces will not be limited by smectite coatings or cements. This is in agreement with a study by [Zhu et al. \(2006\)](#), who concluded that smectite grain coatings were sufficiently porous that they did not occlude or act as diffusive barrier to underlying mineral surfaces. This also agrees also with the results of similar characterization and [numerical modeling](#) of nano-crystalline [chlorite](#) ([Steefel et al., 2015b](#)).



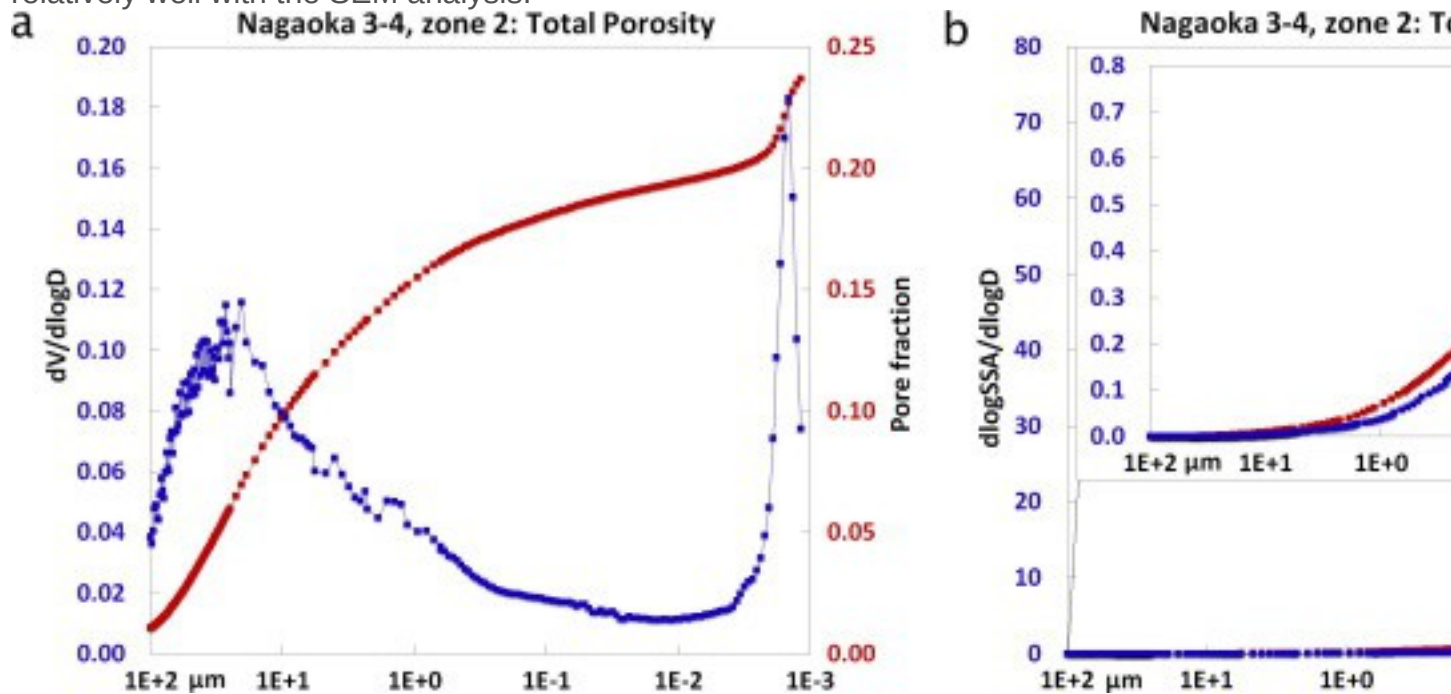
1. [Download high-res image \(332KB\)](#)
2. [Download full-size image](#)

Fig. 2. FIB-SEM images of [smectite](#) showing a single slice (left), the 3D compilation of all 2D slices (middle), and the extracted connected [porosity](#) (right).

### 3.1.3. SANS/USANS

Estimates of porosity from [neutron scattering](#) are pore geometry independent, as is the scale distribution of pores. Calculations of individual pore volume and total surface area are geometry-dependent. Scattering data from thick sections of Nagaoka [reservoir rock](#) show ([Fig. 3a](#)) that there are two pore size distributions. The first is centered at 25 microns, extends from 1 to 100 microns, and contributes a total of 14% porosity (as shown by the cumulative porosity (red) in [Fig. 3a](#)). This part of the distribution captures the pores between grains of quartz, [plagioclase](#), [potassium feldspar](#), [amphibole](#) and other minerals shown in [Fig. 1](#). A second, narrower peak at 1.5 nm is also apparent in these data. It contributes roughly 3% of the total porosity (see cumulative porosity in [Fig. 3a](#)) and is interpreted as being dominated by inter-platelet voids within smectite. Voids within glass can also approach this size range, but are expected to have a far broader size distribution and therefore form a less distinct signal. In the Nagaoka samples, only smectite has both the characteristic geometry and the abundance to be

the primary host for the peak in scattering object volume observed at 1.5 nm. The total porosity (connected and unconnected) in the Nagaoka reservoir rock samples measured is estimated from neutron scattering to be 24% for the spatial range of about 1 nm to 100 microns (red symbols in Fig. 3a). The sample porosity determined from the 0.2 μm resolution SEM images (Section 2.2.1) was 14.7%. The total porosity for pores greater than 0.2 μm from the neutron scattering data (Fig. 3a) is ~12%, which agrees relatively well with the SEM analysis.



1. [Download high-res image \(282KB\)](#)
2. [Download full-size image](#)

Fig. 3. SANS/USANS: Small and ultra small-angle [neutron scattering](#) data, extended using [BSE](#) imagery, for a Nagaoka reservoir sample. The X-axis of all graphs shows [pore size](#) in microns. [Fig. 3a](#) shows cumulative (red) and differential (blue) porosity; differential porosity is normalized by the logarithmic difference between values of the scattering vector  $Q$ . [Fig. 3b](#) shows cumulative and differential surface area, based on a dual-geometry model. Differential surface area is normalized. For clarity, surface areas adjacent to larger pores are scaled up in the inset figure. (For interpretation of the references to color in this figure legend, the reader is referred to the web version of this article.)

Surface area results ([Fig. 3b](#)) highlight the importance of correctly attributing the source, and therefore the geometry and connectedness of micro-pores in the Nagaoka. Virtually all (>96%) of the total surface area observable in the size regime interrogated by neutron scattering is adjacent to scattering objects less than 10 nm in size but larger

than the smallest observable coherent scattering object size, a limit imposed by the incoherent hydrogen scattering signal at about 1 nm. From the pore size distribution of porosity, the total and pore size distribution of surface area is calculated using a model of pore geometry. For this investigation, the dual-geometry model described previously was used. Results from this model were then compared to those from the all-spherical model generally used for scattering studies. A second [sensitivity analysis](#) was then performed on the dual-geometry model by systematically varying model parameters. The total surface area of the Nagaoka reservoir samples studied is estimated using neutron scattering to be 18 m<sup>2</sup>/g, if a dual-geometry model is employed. Virtually all of this surface area consists of objects smaller than 10 nm in size. All objects of such sizes are here modeled as slits. If they were instead modeled as spheres, then the estimate of surface area ( $SA_{est, sphere}$ ) would be

$$(9) SA_{est, sphere} = SA_{est, slit} * SA_{sphere} V_{slit} / SA_{slit} V_{sphere}$$

and therefore reduces to

$$(10) SA_{est, sphere} = SA_{est, slit} * \pi d^2 * d / (r_{slit}^2 * 16 \pi d^3 * 2 \pi r_{slit}^2) = SA_{est, slit} * 3$$

or 54 m<sup>2</sup>/g. Comparison of these results to the BET measured surface area of 23.55 m<sup>2</sup>/g in [Beckingham et al., \(2016\)](#), indicates that the slit-shaped model of nanoscale pores yields a more consistent value.

If the focus of analysis is total surface area, then the only important question for these particular samples is whether nanoscale pores are treated as slits or spheres. However, the distribution of surface area can be significantly altered by sufficiently large adjustments to model parameters. Any model assuming a slit-shaped geometry for pores requires an independent estimate of the size of the [platelets](#) forming the top and bottom surfaces of slit-shaped pores ( $r_{slit}$ ). A dual-geometry model of the type employed for this study adds two additional parameters: the scale of scattering objects at which 50% are assumed to be slits, and the width of the transition zone between spheres and slits. All of these parameters are estimated either from literature values or from examination of other analyses (in particular SEM) on the Nagaoka samples. Sensitivity tests were performed by varying each of these parameters. Because the Nagaoka samples exhibit a clear demarcation between macroscale and nanoscale porosity, and because all plausible estimates for model parameters based on a sandy, smectite-rich sample such as the Nagaoka reservoir cause the first to be treated entirely as spheres, and the second entirely as slits, conclusions about not merely the total surface area, but the size of pores adjacent to most of the total surface area do not change radically. However, estimates from neutron scattering concerning the distribution of the surface

area adjacent to pores of ~50 to 1000 nm, in the transition zone between pores adjacent and not-adjacent to smectite, are less well-constrained.

#### 3.1.4. 2D pore connectivity and mineral accessibility

Given the abundance of smectite cement and coatings in the sample, the accessibility of mineral surfaces needs to account for the connectivity of the micro- and macro-scale porosity. As discussed in Section [3.1.2](#), the smectite contains abundant, well-connected micro-porosity. Therefore, the connected porosity may include connectivity through micro-porous smectite in addition to [macro-pores](#) identified in the segmented BSE images. Using the burning algorithm, connected pore pixels were classified as smectite or BSE identified pore pixels adjacent to burned (smectite or BSE identified) pore pixels. This connected pore space will further be referred to as “connected macro- and meso-pores”. The connected pore space is shown in [Fig. 4](#) in white (connected macro-pores identified in BSE images) and light blue (connected micro-porous smectite). Accessible mineral surfaces are those adjacent to a connected micro- or macro-pore pixel.



1. [Download high-res image \(3MB\)](#)
2. [Download full-size image](#)

Fig. 4. Registered [SEM BSE](#) and QEMSCAN image with multi-scale (macro and micro [pore](#) connectivity analysis. Connected [macro pores](#) are depicted in white and connected micro-porous [smectite](#) regions are depicted in light blue. (For interpretation of the references to color in this figure legend, the reader is referred to the web version of this article.)

Mineral abundance and accessibilities are given in [Table 1](#). The accessible mineral percentages indicate the percentage of the total mineral pixels in contact with the pore space. These values provide the individual mineral contributions to the total accessible surface area. Column B was calculated based on mineral pixels adjacent to pores, as identified in the 2D BSE images, with no consideration of pore connectivity (Section [2.2.1](#)). The adjusted porosity after considering connectivity of the pore space, including connectivity through micro-pores in smectite, is given in Column C.

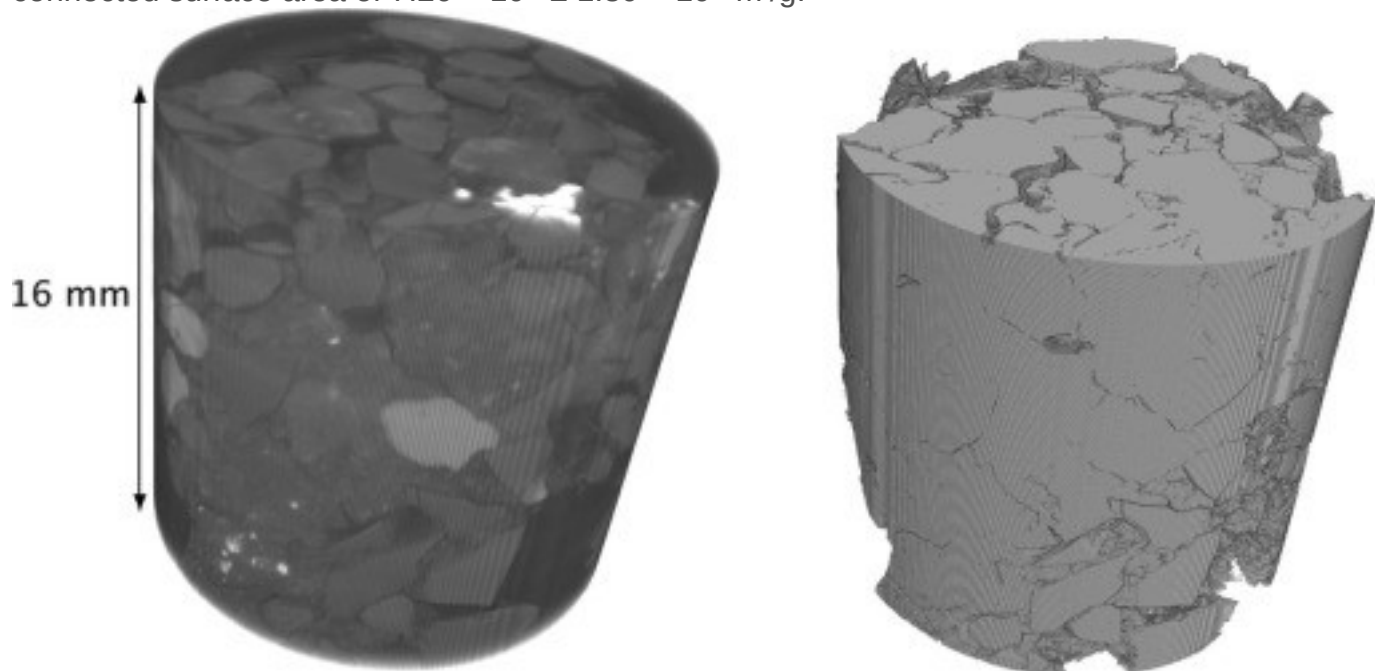
Considering K-feldspar as an example, 8.1% of the total grain pixels adjacent to the total macro pores identified in the 2D BSE image are K-feldspar pixels (Column B). Of the total mineral pixels accessible via connected micro- and macro- pores, 6.9% are K-feldspar (Column C).

[Table 1](#) indicates that the pore accessibility of minerals has a marked effect on what is available for reaction. First, considering the general accessibility of minerals adjacent to macro pores (Columns B vs A), the reported abundances based on the assumption of full accessibility over-estimate the amount of reactive mineral for quartz, plagioclase, K-feldspar, Amphibole, and Fe [Hydroxide](#). As evident in [Fig. 1](#), many of these mineral surfaces are occluded by smectite coatings and cements. In contrast, Column A underestimates the contribution to the accessible surface area of smectite, chlorite, [kaolinite](#), [pyrite](#), [serpentine](#), Ca-phosphate, and [calcite](#). In general, the proportion of clay minerals available for reaction is underestimated by the determinations that neglect pore accessibility as these tend to be present as coatings on other mineral surfaces.

### 3.1.5. Accessible Mineral Surface Areas

The reconstructed and segmented [X-ray](#) CT images of the core are shown in [Fig. 5](#). The average number of pixels of the connected pore surface area from the cuboids was 4,340,381 pixels. The density of the core, computed as 2.55 g/cm<sup>3</sup> from the core dimensions (5 mm × 16 mm length) and weight of 0.8 g, was used to convert the surface area to m<sup>2</sup>/g. The corresponding average cuboid accessible mineral surface

area is  $3.46 \times 10^{-3} \pm 6.2 \times 10^{-4} \text{ m}^2/\text{g}$ , where the error is the 95% *T*-test confidence interval. This connected surface area depends on the imaging resolution used ([Landrot et al., 2012](#)) and is unable to account for features below the voxel resolution. As this sample contains abundant micro-porosity that significantly alters the connectivity of the pore network, a correction factor was employed to account for this. The correction factor was determined from the 2D imaging analyses by comparing pore connectivity with and without micro-scale pores. The total number of connected or accessible pixels at the pore/mineral interface when accounting only for the connected macro-pores in the 2D image is 409,496. The total number of pixels at the pore/mineral interface when accounting for the connected smectite micro-porosity is 8,614,220. Dividing the number of interface pixels that include micro-pores by those without gives a correction factor of 21. Applying this correction factor to the 3D connected surface areas results in a 3D connected surface area of  $7.26 \times 10^{-2} \pm 1.30 \times 10^{-2} \text{ m}^2/\text{g}$ .



1. [Download high-res image \(109KB\)](#)
2. [Download full-size image](#)

Fig. 5. [X-ray](#) CT image of unreacted core (left) and segmented core image (right). The [porosity](#) of the core, computed by counting the total number of pore pixels in the segmented image, is 21.8%. (For interpretation of the references to color in this figure legend, the reader is referred to the web version of this article.)

The accessible mineral surface areas are given in [Table 2](#). These surface areas are determined by multiplying the mineral surface area adjacent to the connected pore network, as determined from 3D X-ray CT images ( $7.26 \times 10^{-2} \text{ m}^2/\text{g}$ ), by the accessible

mineral percentages (column C of [Table 1](#)). For smectite, this results in an accessible surface area of .026 m<sup>2</sup>/g. This accessible surface area, however, does not account for mineral surfaces adjacent to connected micro-pores. From the FIB-SEM analysis, the surface area adjacent to connected micro-pores in smectite is 9.9 m<sup>2</sup>/g. However, only a fraction of the total smectite contributes to the overall connected pore system. The total number of smectite pixels (purple pixels in [Fig. 1](#)) is  $3.33 \times 10^7$  and the total number of connected smectite pixels (light blue pixels in [Fig. 4](#)) is  $3.12 \times 10^7$ . The percentage of smectite micro-pores that are a part of the overall connected pore network is 93.9% which corresponds to an accessible surface area of 9.3 m<sup>2</sup>/g. This surface area is added to the accessible surface area above for a total smectite accessible surface area of 9.33 m<sup>2</sup>/g.

Table 2. Mineral specific surface areas computed using 2D image perimeter method in [Beckingham et al. \(2016\)](#) (Image perimeter SSA), multi-scale image obtained accessible surface areas (Image accessible SA, Section [3.1.4](#)), and the corresponding scaling factor relating specific and accessible surface areas. Details on the computation of image accessible surface area error can be found in [Appendix D](#).

Mineral	Volume %	Image perimeter SSA, (m <sup>2</sup> /g)	Image accessible SA (m <sup>2</sup> /g)	Scaling factor (S <sub>acc</sub> )
Quartz	27.64	0.089	9.95E-03 +/- 2.04E-03	0.11
Plagioclase	21.4	0.109	1.06E-02 +/- 2.85E-03	0.05
Albite	6.46			
An25	1.49			
Labradorite	13.46			
Smectite	16.99	136.3	9.33 +/- 3.26	0.068
K-feldspar	14.62	0.146	4.98E-03 +/- 1.16E-03	0.034
Pyroxene	7.21	0.214	8.06E-03 +/- 1.88E-03	0.037
Fe,Mg rich	5.46			
Ca,Mg rich	1.72			
AlSitrup	2.74	0.482	2.71E-03	0.0056
Biotite	2.58	4.74	3.75E-03 +/- 1.01E-03	0.0078
Amphibole	1.85	0.234	1.41E-03 +/- 3.29E-04	0.006
Others	1.42	0.498	1.92E-03	0.0038
Fe Hydroxide	1.22	0.195	5.94E-04 +/- 1.59E-04	0.003
Chlorite	1.17	7.6	9.49E-04 +/- 2.92E-04	0.0012
Kaolinite	0.41	13.2	8.79E-04 +/- 3.07E-04	0.00065
Pyrite	0.36	0.149	1.68E-04 +/- 6.60E-05	0.00011
Serpentine	0.29	7.15	2.26E-04	0.000029
Ca-phosphate	0.07	0.274	4.02E-05 +/- 1.58E-05	0.000005
Calcite	0.03	0.281	2.14E-05 +/- 1.14E-05	0.00000076

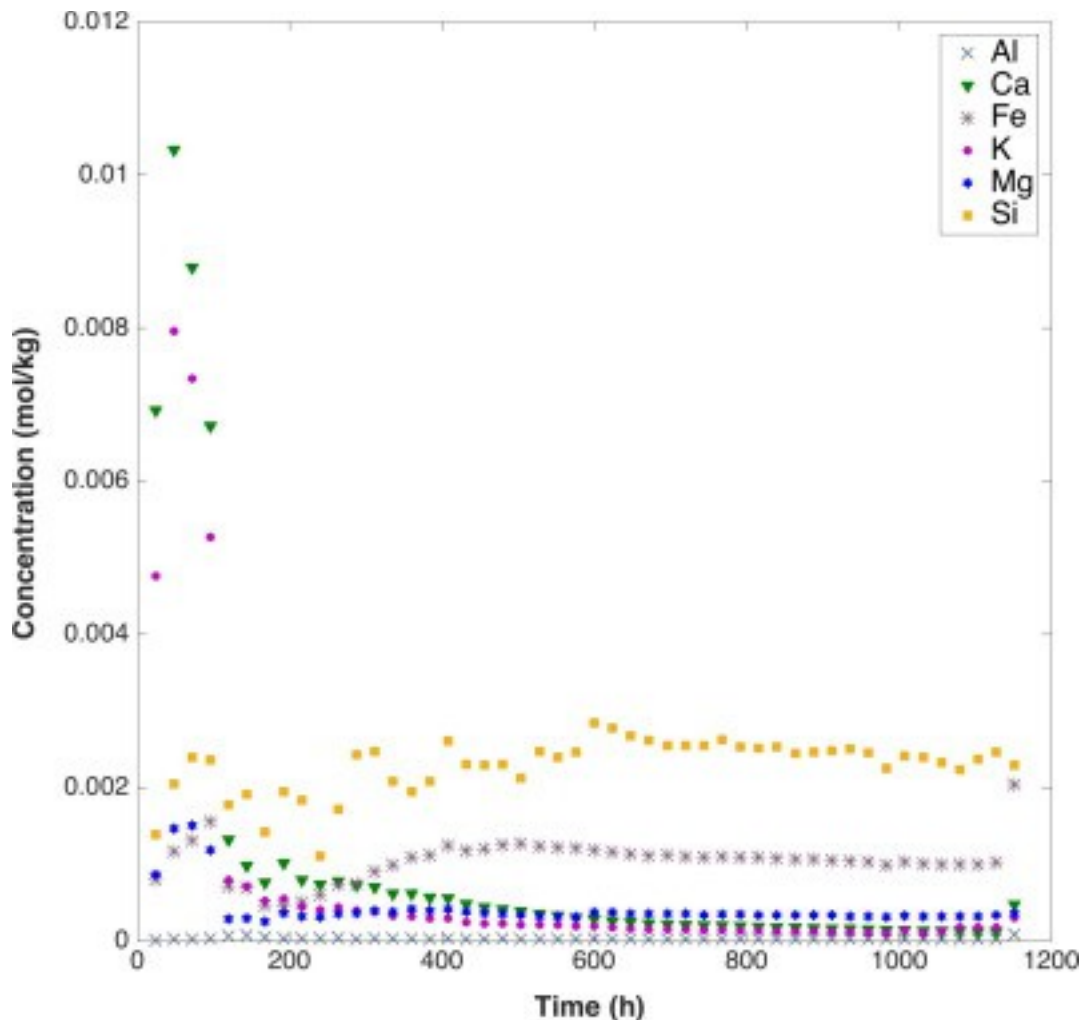
Accessible surface areas for non-clay minerals range from  $10^{-2}$  to  $10^{-5}$  m<sup>2</sup>/g and are, in general, one or more orders of magnitude below the image perimeter specific surface areas. Variations in specific and accessible surface area can be easily compared by considering the scaling factor (SF) between the two surface areas where

(11) accessible surface area = SF \* specific surface area

Mineral scaling factors are also given in [Table 2](#). Scaling factors appear to be a function of mineral abundance, with the least abundant minerals having the scaling factors that range up to five orders of magnitude. Scaling factors for the more abundant minerals (>5%) range between one to two orders of magnitude.

### 3.2. Core flood dissolution experiment

[Effluent ion concentrations](#) from the core flood dissolution experiment are shown in [Fig. 6](#). Ca<sup>2+</sup> and K<sup>+</sup> exhibit the highest initial peaks in concentration followed by rapid decrease and apparent approach to steady-state after approximately 600 h. Mg<sup>2+</sup> also shows a peak in concentration at early times followed by rapid approach to apparent steady-state. SiO<sub>2</sub> and Fe show high concentrations at early time, which then increase continuously after 200 h. pH was not measured in the effluent because of degassing of CO<sub>2</sub> once the solution was collected in open containers, but [reactive transport](#) simulations suggest an increase to about 3.68 from the injection value of about 3.20.



1. [Download high-res image \(174KB\)](#)
2. [Download full-size image](#)

Fig. 6. [Effluent cation](#) concentrations measured from the flow-through core experiment.

### 3.3. Reactive transport modeling

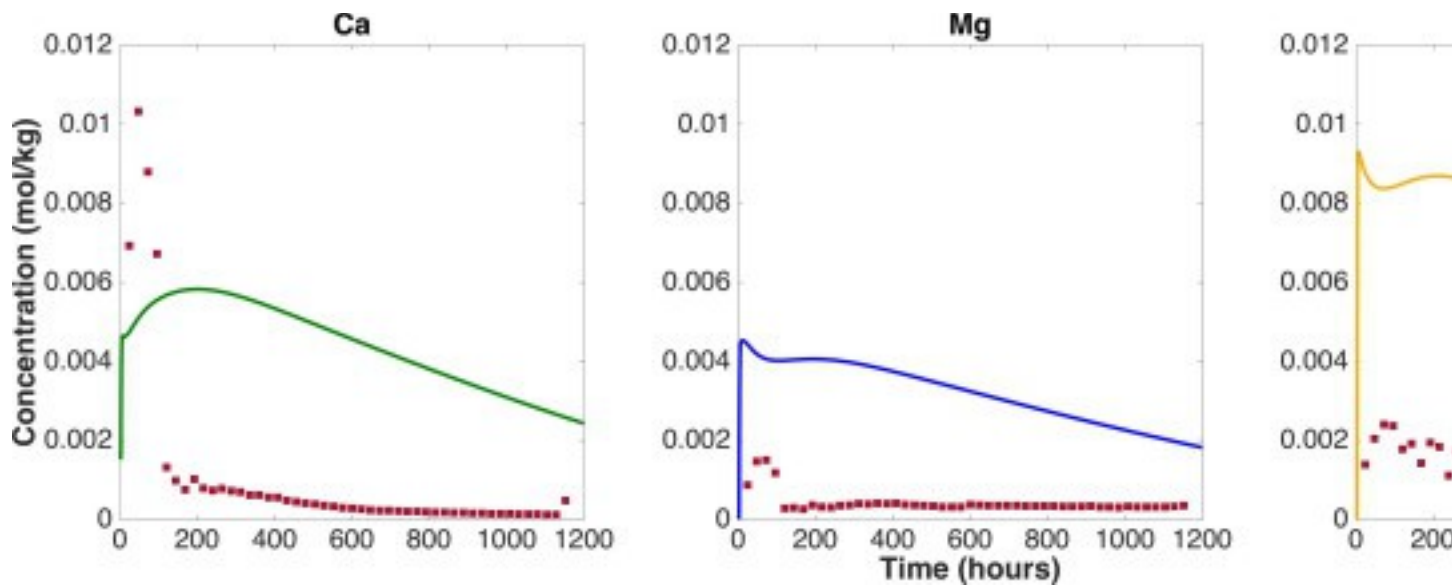
#### 3.3.1. Simulations using 'best-fit' disaggregated sediment surface areas

Typically, continuum reactive transport simulations do not consider explicitly the accessibility of mineral surfaces, but instead use specific or geometric surface areas as estimates of mineral reactive surface area to account implicitly for this effect. The need to account for mineral accessibility explicitly and quantitatively is evaluated here by first simulating reaction rates assuming all mineral surfaces are accessible. This model uses the mineral abundances and surface area values that provided the best-fit with the disaggregated experiment effluent concentrations presented in [Beckingham et al. \(2016\)](#), with other parameters (flow rate, porosity, sediment to solution ratio) corrected

for the core flood experiment. The chemistry (including  $p\text{CO}_2$ ) and temperature of the two experiments is also the same. In the disaggregated sediment study, effluent concentrations (and dissolution rates) were successfully simulated using specific mineral surface areas determined from an image perimeter analysis of the 2D SEM registered image above ([Fig. 1](#)). Of course, the full accessibility of the reactive grains makes sense for this case in that the sediment was disaggregated (the pore structure was destroyed) and the reactor was well-mixed. The disaggregated study in [Beckingham et al. \(2016\)](#) also reported high initial [cation](#) peaks and cation to Si ratios resulting from cation leaching and dissolution of a highly-reactive glass phase, as was observed for glass dissolution by [Aradóttir et al. \(2013\)](#). As in the initial well-mixed reactor study, this glass phase (similar in composition to basaltic glass, although with cation leaching preferentially at early times) is also included in the core flood simulations presented here. The dissolution of this glass phase is given by

$$(12)\text{Ca}_{0.98}\text{Al}_{0.18}\text{Si}_{1.6}\text{Na}_{0.02}\text{Fe}_{0.25}\text{Mg}_{0.65}\text{O}_{3.2}\cdot(\text{H}_2\text{O})_{2.16}+4.32\text{H}^+\rightarrow 0.98\text{Ca}^{+++}+0.18\text{Al}^{+++}+1.6\text{SiO}_2(\text{aq})+0.02\text{Na}^{++}+0.25\text{Fe}^{+++}+0.65\text{Mg}^{+++}+2.16\text{H}_2\text{O}$$

where the [stoichiometry](#) was obtained by matching the early time behavior in the effluent chemistry ([Beckingham et al., 2016](#)). The [grain size](#) distribution of minerals discussed in [Beckingham et al. \(2016\)](#) is also included in this core flood simulation. Simulated effluent concentrations using the 'best-fit' disaggregated surface areas from [Beckingham et al. \(2016\)](#) are shown as solid lines in [Fig. 7](#). As can be seen in [Fig. 7](#), the simulations over-estimate the observed effluent concentrations (circles) at all times, with the exception of the Ca peak at earliest time (<100 h). In the simulations, high initial concentration peaks before 400 h are followed by continual declines in effluent concentrations for all cations. Experimentally observed effluent concentrations, however, peak earlier in time for Ca and Mg, while Si has no initial peak and instead increases continuously with time. As the experimentally observed effluent concentrations are lower than the simulated concentrations, it is clear that the assumption that all minerals are accessible in the core sample is incorrect. The fact that these surface areas successfully simulated the disaggregated experiment effluent concentrations in [Beckingham et al. \(2016\)](#) strongly suggests that accounting for mineral accessibility is necessary to describe reactivity in sediments with their pore structure intact.



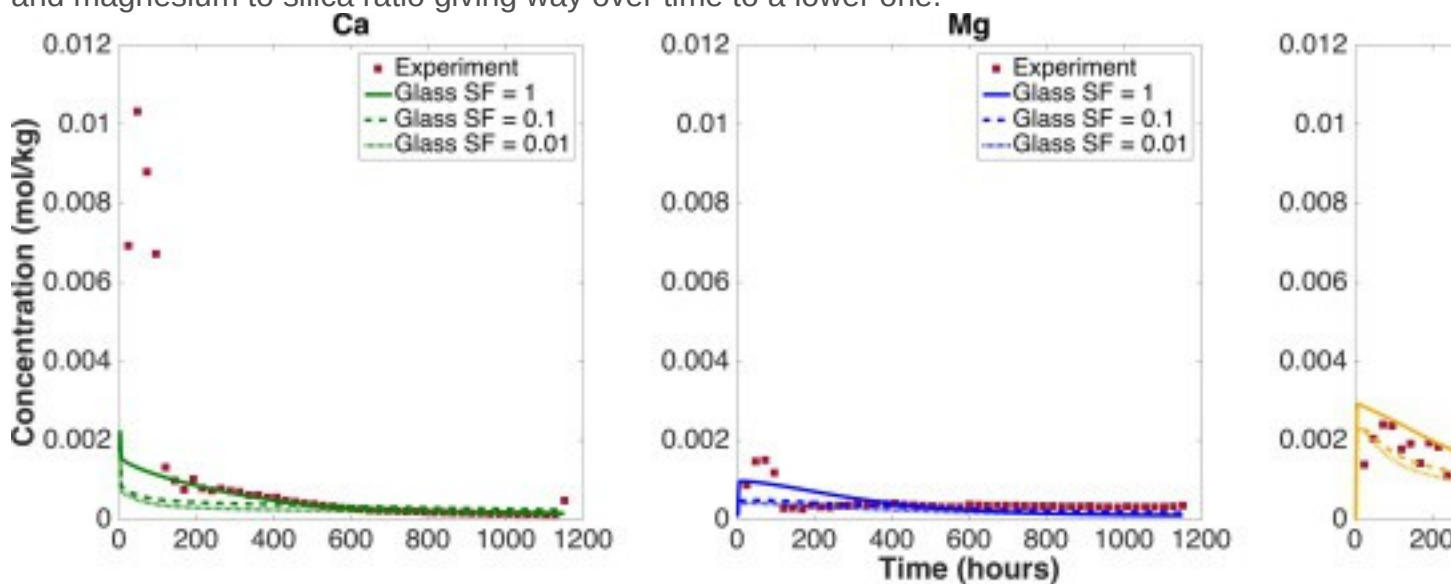
1. [Download high-res image \(183KB\)](#)
2. [Download full-size image](#)

Fig. 7. Observed (squares) and simulated [effluent](#) Ca, Mg, and Si concentrations (lines) using image-perimeter obtained specific surface areas from a well-stirred, disaggregated sediment experiment reported in [Beckingham et al. \(2016\)](#).

The [quasi-steady state](#) concentration of Al was approximately 20  $\mu\text{mol/L}$  and speciation calculations with the reactive transport software indicate that the minerals [gibbsite](#) and [boehmite](#) were slightly supersaturated at the end of the column due to the rise in pH to about 3.68 from the injection value of about 3.2. This would contribute to Al retention in the column, but would not affect the solubility of the highly soluble phases controlling the rest of the effluent chemistry (plagioclase, [pyroxene](#), glass). There was no attempt to model the Al behavior. Fe averaged about 1 mM ([Fig. 6](#)), but the mineral [goethite](#) (the most stable) remains undersaturated throughout the column. To capture the Fe behavior, it was necessary to include a dissolving Fe-hydroxide phase, although given the uncertainty in the glass composition, detailed simulation of the Fe was not pursued. The ions  $\text{Na}^+$  and  $\text{Cl}^-$  were included in the simulations, but given their high background of 0.1 M, there was no attempt to simulate their behavior in the experiments. pH increased in the simulations from the injection value of 3.20 to about 3.68 (depending on the simulation), although pH was not directly measured due to  $\text{CO}_2$  degassing in the open containers used to collect the effluent. Cation exchange was included in all of the simulations, but resulted in only a short-lived pulse of the cations  $\text{Ca}^{++}$  and  $\text{Mg}^{++}$  over several pore volumes. This effect cannot be used to explain the long-lived but continuously declining cation concentrations (up to 300 h).

### 3.3.2. Simulations using accessible surface areas

Simulated effluent cation concentrations using the multi-scale image-derived accessible surface area values (Table 2) are shown as a solid line in Fig. 8. These simulated concentrations based on accessible surface areas are much closer than the disaggregated sediment-derived surface areas to the experimentally observed values. Fig. 8 compares the simulated and experimental  $\text{Ca}^{2+}$ ,  $\text{Mg}^{2+}$ , and  $\text{SiO}_2$  data using a range of scaling factors for the single glass phase (no scaling of other mineral phase specific surface areas) that was included in Beckingham et al. (2016). The accessible glass surface area is computed from equation 11 using scaling factors of 1.0, 0.1, and 0.01. Using the same glass surface area as the disaggregated sediment best fit value (scaling factor of 1.0) produces a good early match of the calcium effluent concentration, a reasonable match with the early magnesium behavior, and then a poor match with the Si. In particular, the simulations cannot capture the rise in Si concentration over time, and generally under-predict the steady state concentrations, since the glass is depleted at late time. The lower glass scaling values of 0.1 and 0.01 perform slightly better in capturing the steady state (late time) values because the reactive glass phase is depleted more slowly in the case of the reduced glass surface area. The under-prediction of the steady state values, however, suggests the glass concentration in the core is higher than in the disaggregated sediment, in addition to having a higher silica content in the glass phase. Cation leaching was apparently an important effect in the disaggregated sediment experiment, with an early high calcium and magnesium to silica ratio giving way over time to a lower one.



1. [Download high-res image \(236KB\)](#)

## 2. [Download full-size image](#)

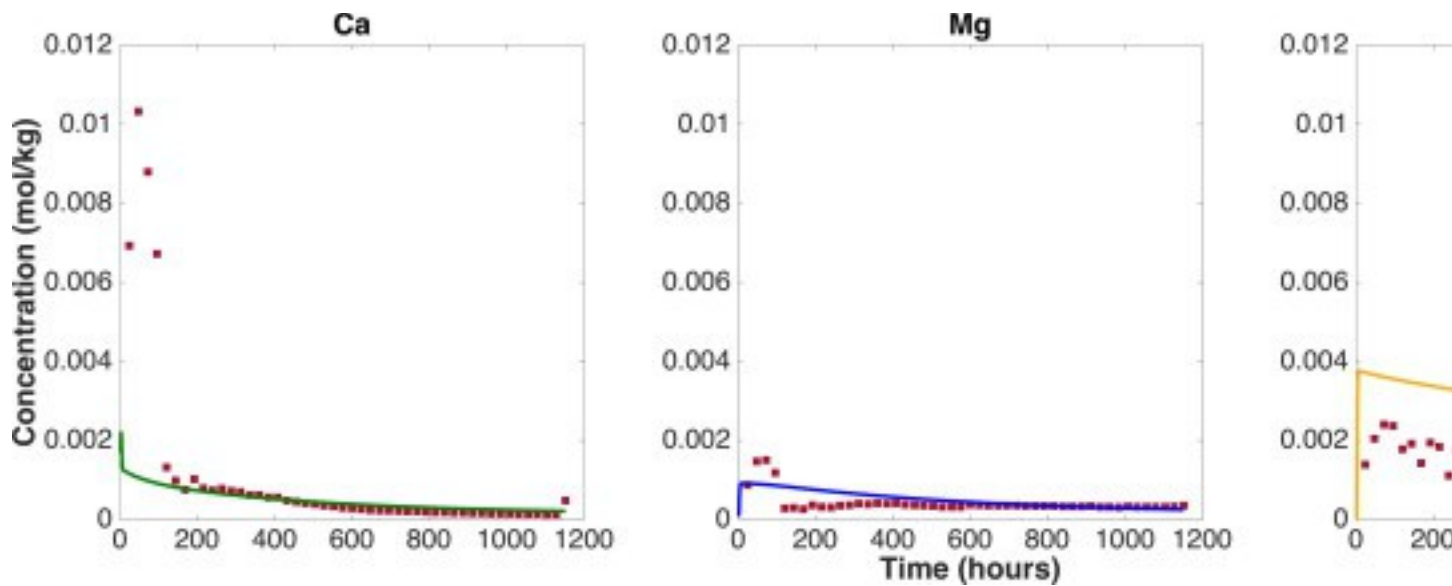
Fig. 8. [Effluent ion concentrations](#) for simulations run using image-obtained accessible surface areas and a single glass phase and a range of scaling factors for the glass. All other reactive surface areas are as given in [Table 2](#).

### 3.3.2.1. Simulations with two glass compositions

The less than perfect fit of the simulations using the image-accessible surface areas to the steady state values suggests that a second glass phase with a differing composition (higher in silica) is present, or that a single glass phase undergoes a more complex leaching behavior that involves dissolution of high [silica glass](#) after the initial cation leaching phase. In this simulation, this is explored through the addition of a second distinct glass phase. There seem to be no other possible sources of silica here, since the dissolution rate required to produce this high silica would exceed that of any common silica-bearing phase. The composition of the first glass phase is the same as in [Beckingham et al. \(2016\)](#) (Eq. (12)), while the composition of the second glass phase is interpreted to be



based on matching of the effluent chemistry. As before, the actual stoichiometry of the glass is not based on direct chemical analysis, but is based rather on matching the effluent chemistry. The best fit values of the [volume fractions](#) of the first (high Ca and Mg) glass and the second (high silica) glass are 0.07% and 1.3%, respectively. The corresponding best fit surface areas are 0.15 m<sup>2</sup>/g and 0.70 m<sup>2</sup>/g. Simulated effluent ion concentrations using the two glasses are shown in [Fig. 9](#). Note that the behavior at long times where the system approaches a quasi-steady state is dominated by the crystalline material that is present, and not the glass.



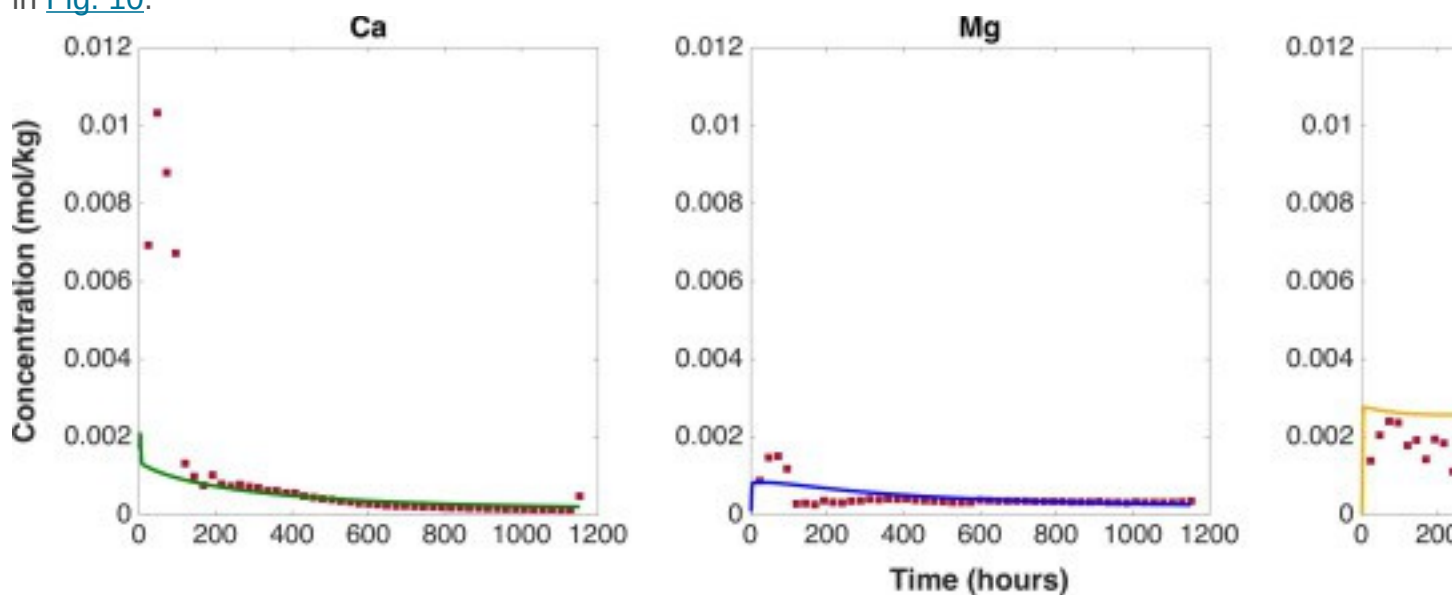
1. [Download high-res image \(162KB\)](#)
2. [Download full-size image](#)

Fig. 9. Experimentally observed (solid squares) and simulated (lines) [effluent ion concentrations](#) using accessible [mineral surface](#) areas and two glass compositions.

### 3.3.2.2. Simulations with armoring

While the simulations using two distinct glass phases are able to provide a relatively good fit with the observed Ca and Mg experimental effluents, they are unable to match observed Si effluent concentrations, and in particular, the increase in silica effluent concentrations late in the experiment. The simulations over-predict the early silica concentrations and fail to capture the late (>200 h) increase in concentration. The lower initial silica concentrations and the later increase suggest that a model that couples the two glass phases (high Ca + Mg early, and high Si late) through an armoring mechanism might be appropriate, with the higher silica glass undergoing dissolution only once the high Ca + Mg glass phase is depleted. In the simulations, if the high silica glass is allowed to dissolve immediately, the non-monotonic effluent silica behavior with its late peak cannot be matched. Alternatively, this complex behavior might be the result of the formation of a cation leached layer in which Ca and Mg are released earlier, while Si is retained in the leached layer until steady state diffusion-controlled dissolution of the glass phase is achieved (e.g. [Steefel et al., 2015b](#)). While this second cation leaching model might capture the gradually decreasing (Ca + Mg)/Si ratio, it is difficult or impossible to produce an increase in absolute Si concentration with this mechanism. Another possible explanation might be that the core sample disaggregates progressively as a result of dissolution, increasing the accessibility of the sample over

time. Further disaggregation of the sample would result in an increase in effluent ion concentrations with time, as observed for Si, essentially driving the core flood experiment toward the physical conditions of the disaggregated sediment experiment. The primary argument against this explanation is that it would tend to predict similar increases in Ca and Mg effluent concentrations as the reactive pyroxene and plagioclase grains dominate the effluent chemistry at late times. Explanations involving smectite dissolution do not seem likely, since this phase dissolves too slowly to produce these kind of high silica concentrations for the experimental flow rates (and thus residence times) involved. Thus, dissolution of a second Si-rich glass phase that is armored or coated by the Ca + Mg glass phase included in the disaggregated sediment simulations seems the likeliest explanation. With this mechanism, the Si-rich glass only begins to dissolve at a faster rate once the Ca + Mg glass is depleted, improving the fit of the Si over the early and later periods of dissolution in the core experiment as shown in [Fig. 10](#).



1. [Download high-res image \(158KB\)](#)
2. [Download full-size image](#)

Fig. 10. Comparison of experimental (solid squares) and simulated (solid lines) [effluent](#) concentrations using two glass compositions and including armoring of a relatively higher Si glass by the high Ca + Mg glass included in [Beckingham et al. \(2016\)](#).

#### 4. Discussion

As discussed above, mineral abundance does not necessarily reflect the distribution of minerals accessible for reaction. When [clay minerals](#) are present, they may exist as

grain surface coatings or cementing material as observed here and in previous studies ([Peters, 2009](#), [Landrot et al., 2012](#), [Waldmann et al., 2014](#)). As a result, clay minerals are more accessible to the [pore space](#). In contrast, the clay mineral coatings may reduce the accessibility and effective [mineralogy](#) of other minerals. [Pore](#) connectivity may also alter the relative proportion of minerals available for reaction as observed here and in [Landrot et al. \(2012\)](#). In samples with abundant clay content, the connectivity of the nano-scale pores can significantly contribute to the overall connected porosity. This is the case for the [smectite](#) micro-pores characterized here and [chlorite](#) micro-pores in [Landrot et al. \(2012\)](#). Understanding the extent and connectivity of clay micro-pores in grain coatings is also needed to assess if underlying [mineral surfaces](#) will be accessible to reactive fluids. The abundant, well-connected micro-pores in smectite observed in the analysis above will not likely completely occlude the reactivity of the underlying mineral surface, although it may contribute to a slowing of [solute transport](#) to and from reactive grains coated by the clay. This, however, may be sample specific and further investigation is needed to determine if this will be true for all smectite grain coatings.

Nano-scale features in clay minerals may also account for a majority of the specific surface area. As evident in this sample from the FIB-SEM, (U)SANS, and analysis in [Beckingham et al. \(2016\)](#), the nano-scale features in smectite contribute a large fraction of the total specific surface area (23.55 m<sup>2</sup>/g measured by BET analysis in [Beckingham et al. \(2016\)](#)). However, in this study the smectite dissolves too slowly to produce the observed [effluent](#) concentrations.

[Reactive transport](#) simulations of the core experiment demonstrate that the use of reactive surface area estimates assuming all mineral surfaces are accessible, as in the best-fit matches of the disaggregated Nagaoka sediment experiment reported in [Beckingham et al. \(2016\)](#), over-estimates the extent and rate of mineral dissolution. In this study, we have shown that an explicit and quantitative incorporation of the pore accessibility of reactive phases improves the ability to simulate effluent chemistry from an experimental core flood experiment in which the sediment retains its pore structure. In comparing results of the disaggregated sediment and intact core experiment, it was necessary to include a second glass phase with a higher Si composition. Whether in fact this is a distinct glass phase (i.e., chemical heterogeneity), or whether it is a more complex development of a leached layer in the glass is not completely clear, but an armoring mechanism is proposed to capture the increase in absolute Si concentration in the effluent at late times. The required inclusion of both glass composition and armoring

highlights the challenges of accurately modeling dissolution and mineralization in volcanogenic clastics similar to the Haizume formation.

At the field site, increases in Ca, Mg, Fe, and Si concentrations were observed after one year, as described in [Mito et al. \(2008\)](#). Using reactive transport simulations, they attributed the observed concentration increases to dissolution of [plagioclase](#), chlorite and carbonate minerals ([Mito et al., 2008](#)). In comparison with the core flood experiment carried out here, a much higher Ca/Si ratio was observed at the field site. This is likely because of the low chlorite and carbonate mineral [volume fractions](#) in the core sample. Ultimately, accounting for the accessibility of mineral surfaces is critical to match the experimentally observed effluent concentrations. In this case, simulations using reactive surface areas that assume all mineral surfaces are accessible over-estimated the extent and rate of mineral reaction. This is because some of the more reactive mineral surfaces (pyroxene, plagioclase, and K-feldspar) are actually occluded and not accessible for reaction. The modeling of the core flood experimental data suggest a factor of 10–20 reduction in reactive surface area (relative to the disaggregated sediment values) is required. We suggest that this might be taken as a typical reduction in RSA for poorly cemented and sorted sediment like that occurring at the Nagaoka site. We observe less (or no) reduction is needed for well sorted and uncemented samples (e.g., [Noiriel et al., 2012](#)), and expect that more strongly cemented sediments or rocks may require a more significant reduction in RSA because of the even more limited pore accessibility of reactive phases in such materials. However, additional data is needed to verify this hypothesis.

In the context of CO<sub>2</sub> sequestration, failing to properly account for the accessibility of mineral reactive surface areas could result in erroneous estimates of the extent and rate of mineral reactions. If reactive minerals are more accessible for reaction than is estimated by their mass or volume fractions, mineral dissolution would be underestimated in model simulations that do not account for accessibility. This could result in underestimating the rate and extent of CO<sub>2</sub> mineral trapping, as the release of the necessary [cations](#) for carbonates would in turn be underestimated. As mineral dissolution and precipitation reactions can alter formation porosity and permeability, and thus the injection and subsequent [fluid flow](#) rates, it is important to be able to predict subsurface mineral reactivity accurately. Similar comments can be made about the importance of accessibility in determining mineral dissolution rates in other environments, for example, [chemical weathering](#) at the Earth's surface or reactive fracture evolution as minerals at the fracture surface react.

## Acknowledgements

This work was supported as part of the Center for Nanoscale Control of Geologic CO<sub>2</sub> (NCGC), an Energy Frontier Research Center funded by the U.S. Department of Energy, Office of Science, Basic Energy Sciences under Award # DE-AC02-05CH11231. [X-ray Micro Tomography](#) experiments were performed with the assistance of Dula Parkinson and Alastair MacDowell at the Advanced Light Source, Beamline 8.3.2, which is supported by the Office of Science, Office of Basic Energy Sciences, of the U.S. DOE (contract [DE-AC02-05CH11231](#)). FIB/SEM studies were performed at the Nanofabrication Facility within the Molecular [Foundry](#) (LBNL) which is supported by the Office of Science, Office of Basic Energy Sciences, of the U.S. DOE (contract DE-AC02-05CH11231). Rock sample collection at the Nagaoka pilot CO<sub>2</sub> injection site was financed by Ministry of Economy, Trade and Industry (METI) under the contract of “Research and Development of [Underground Storage](#) for Carbon Dioxide”. We also acknowledge the support of the National Institute of Standards and Technology, Center for [Neutron](#) Research, the U.S. Department of Commerce in providing the research neutron facilities used in this work. This work used facilities supported in part by the NSF under agreement no. DMR-0944772. Certain commercial equipment, instruments, materials, and software are identified in this paper to foster understanding. Such identification does not imply recommendation or endorsement by the National Institute of Standards and Technology, nor does it imply that the materials or equipment identified are necessarily the best available for the purpose.

## Appendix A. Supplementary data

[Download Word document \(28KB\)Help with docx files](#)

Supplementary data 1.

## References

### [Anovitz and Cole, 2015](#)

L.M. Anovitz, D.R. Cole **Characterization and analysis of porosity and pore structures**  
Rev. Mineral. Geochem., 80 (2015), pp. 61-164

[CrossRefView Record in Scopus](#)

### [Anovitz et al., 2009](#)

L.M. Anovitz, G.W. Lynn, D.R. Cole, G. Rother, L.F. Allard, W.A. Hamilton, L. Porcar, M.-H. Kim **A new approach to quantification of metamorphism using ultra-small and small angle neutron scattering**

Geochim. Cosmochim. Acta, 73 (2009), pp. 7303-7324

[ArticleDownload PDFView Record in Scopus](#)

[Anovitz et al., 2013](#)

L.M. Anovitz, D.R. Cole, G. Rother, L.F. Allard, A.J. Jackson, K.C. Littrell **Diagenetic changes in macro- to nano-scale porosity in the St. Peter Sandstone: an (ultra) small angle neutron scattering and backscattered electron imaging analysis**

Geochim. Cosmochim. Acta, 102 (2013), pp. 280-305

[ArticleDownload PDFView Record in Scopus](#)

[Aradóttir et al., 2013](#)

E.S.P. Aradóttir, B. Sigfússon, E.L. Sonnenthal, G. Björnsson, H. Jónsson **Dynamics of basaltic glass dissolution – capturing microscopic effects in continuum scale models**

Geochim. Cosmochim. Acta, 121 (2013), pp. 311-327

[ArticleDownload PDFView Record in Scopus](#)

[Atchley et al., 2014](#)

A.L. Atchley, A.K. Navarre-Sitchler, R.M. Maxwell **The effects of physical and geochemical heterogeneities on hydro-geochemical transport and effective reaction rates**

J. Contam. Hydrol., 165 (2014), pp. 53-64

[ArticleDownload PDFView Record in Scopus](#)

[Barker et al., 2005](#)

J.G. Barker, C.J. Glinka, J.J. Moyer, M.H. Kim, A.R. Drews, M. Agamalian **Design and performance of a thermal-neutron double-crystal diffractometer for USANS at NIST**

J. Appl. Crystallogr., 38 (2005), pp. 1004-1011

[CrossRefView Record in Scopus](#)

[Béarat et al., 2006](#)

H. Béarat, M.J. McKelvy, A.V.G. Chizmeshya, D. Gormley, R. Nunez, R.W. Carpenter, K. Squires, G.H. Wolf **Carbon sequestration via aqueous olivine mineral carbonation: role of passivating layer formation**

Environ. Sci. Technol., 40 (2006), pp. 4802-4808

[CrossRefView Record in Scopus](#)

[Beckingham et al., 2016](#)

L.E. Beckingham, E.H. Mitnick, C.I. Steefel, S. Zhang, M. Voltolini, A.M. Swift, L. Yang, D.R. Cole, J.M. Sheets, J.B. Ajo-Franklin, D.J. DePaolo, S. Mito, Z. Xue **Evaluation of mineral reactive surface area estimates for prediction of reactivity of a multi-mineral sediment**

Geochim. Cosmochim. Acta, 188 (2016), pp. 310-329

[ArticleDownload PDFView Record in Scopus](#)

[Bourg et al., 2015](#)

I.C. Bourg, L.E. Beckingham, D.J. DePaolo **The nanoscale basis of CO<sub>2</sub> trapping for geologic storage**

Environ. Sci. Technol., 49 (2015), pp. 10265-10284

[CrossRefView Record in Scopus](#)

[Brantley et al., 2008](#)

S.L. Brantley, J.D. Kubicki, A.F. White (Eds.), Kinetics of Water-Rock Interaction, Springer, New York, NY (2008)

[Chiyonobu et al., 2013](#)

S. Chiyonobu, T. Nakajima, Y. Zhang, T. Tsuji, Z. Xue **Effect of reservoir heterogeneity of haizume formation, nagaoka pilot site, based on high-resolution sedimentological analysis** Energy Proc., 37 (2013), pp. 3546-3553

[ArticleDownload PDFView Record in Scopus](#)

[Crandell et al., 2012](#)

L.E. Crandell, C.A. Peters, W. Um, K.W. Jones, W.B. Lindquist **Changes in the pore network structure of Hanford sediment after reaction with caustic tank wastes**

J. Contam. Hydrol., 131 (2012), pp. 89-99

[ArticleDownload PDFView Record in Scopus](#)

[Dierick et al., 2004](#)

M. Dierick, B. Masschaele, L. Van Hoorebeke **Octopus, a fast and user-friendly tomographic reconstruction package developed in LabView®**

Meas. Sci. Technol., 15 (2004), pp. 1366-1370

[CrossRefView Record in Scopus](#)

[G  
a  
n  
o  
r  
-  
e  
t  
-  
a  
l  
-  
2  
0](#)

J. Ganor, E. Roueff, Y. Erel, J.D. Blum **The dissolution kinetics of a granite and its minerals—Implications for comparison between laboratory and field dissolution rates**

Geochim. Cosmochim. Acta, 69 (2005), pp. 607-621

[ArticleDownload](#) [PDFView](#) [Record in Scopus](#)

[Gaus et al., 2008](#)

I. Gaus, P. Audigane, L. André, J. Lions, N. Jacquemet, P. Durst, I. Czernichowski-Lauriol, M. Azaroual **Geochemical and solute transport modelling for CO<sub>2</sub> storage, what to expect from it?**

Int. J. Greenh. Gas Con., 2 (2008), pp. 605-625

[ArticleDownload](#) [PDFView](#) [Record in Scopus](#)

[Gouze and Luquot, 2011](#)

P. Gouze, L. Luquot **X-ray microtomography characterization of porosity, permeability and reactive surface changes during dissolution**

J. Contam. Hydrol., 120–121 (2011), pp. 45-55

[ArticleDownload](#) [PDFView](#) [Record in Scopus](#)

[Lai et al., 2015](#)

P. Lai, K. Moulton, S. Krevor **Pore-scale heterogeneity in the mineral distribution and reactive surface area of porous rocks**

Chem. Geol., 411 (2015), pp. 260-273

[ArticleDownload](#) [PDFView](#) [Record in Scopus](#)

[Landrot et al., 2012](#)

G. Landrot, J.B. Ajo-Franklin, L. Yang, S. Cabrini, C.I. Steefel **Measurement of accessible reactive surface area in a sandstone, with application to CO<sub>2</sub> mineralization**

Chem. Geol., 318–319 (2012), pp. 113-125

[ArticleDownload](#) [PDFView](#) [Record in Scopus](#)

[Littrell et al., 2008](#)

K.C. Littrell, K.M. Atchley, G. Cheng, Y.B. Melnichenko, G.D. Wignall **General Purpose small-angle neutron scattering instrument on HFIR Oak Ridge**

Neutron News, 19 (2008), pp. 20-21

[CrossRefView](#) [Record in Scopus](#)

[Liu et al., 2012](#)

F. Liu, P. Lu, C. Griffith, S.W. Hedges, Y. Soong, H. Hellevang, C. Zhu **CO<sub>2</sub>-brine-caprock interaction: reactivity experiments on Eau Claire shale and a review of relevant literature**

Int. J. Greenh. Gas Con., 7 (2012), pp. 153-167

[ArticleDownload](#) [PDFView](#) [Record in Scopus](#)

[Liu et al., 2015](#)

C. Liu, Y. Liu, S. Kerisit, J. Zachara **Pore-scale process coupling and effective surface reaction rates in heterogeneous subsurface materials**

Rev. Mineral. Geochem., 80 (2015), pp. 191-216

[CrossRef](#) [View Record in Scopus](#)

[Luquot and Gouze](#)

L. Luquot, P. Gouze **Experimental determination of porosity and permeability changes induced by injection of CO<sub>2</sub> into carbonate rocks**

Chem. Geol., 265 (2009), pp. 148-159

[Article Download PDF](#) [View Record in Scopus](#)

[MacDowell et al.](#)

MacDowell, A.A., Parkinson, D.Y., Haboub, A., Schaible, E., Nasiatka, J.R., Yee, C.A., Jameson, J.R., Ajo-Franklin, J.B., Brodersen, C.R., McElrone, A.J., 2012. X-ray micro-tomography at the Advanced Light Source. In *Presented at the SPIE Optical Engineering+ Applications*, pp. 850618–850618.

[Maher et al., 2009](#)

K. Maher, C.I. Steefel, A.F. White, D.A. Stonestrom **The role of reaction affinity and secondary minerals in regulating chemical weathering rates at the Santa Cruz Soil Chronosequence**

California. Geochim. Cosmochim. Acta, 73 (2009), pp. 2804-2831

[Article Download PDF](#) [View Record in Scopus](#)

[Metz et al., 2005](#)

V. Metz, H. Raanan, H. Pieper, D. Bosbach, J. Ganor **Towards the establishment of a reliable proxy for the reactive surface area of smectite**

Geochim. Cosmochim. Acta, 69 (2005), pp. 2581-2591

[Article Download PDF](#) [View Record in Scopus](#)

[Mito et al., 2008](#)

S. Mito, Z. Xue, T. Ohsumi **Case study of geochemical reactions at the Nagaoka CO<sub>2</sub> injection site**

Japan. Int. J. Greenh. Gas Con., 2 (2008), pp. 309-318

[Article Download PDF](#) [View Record in Scopus](#)

[Mito et al., 2013](#)

S. Mito, Z. Xue, T. Sato **Effect of formation water composition on predicting CO<sub>2</sub> behavior: a case study at the Nagaoka post-injection monitoring site**

Appl. Geochem., 30 (2013), pp. 33-40

[Article Download PDF](#) [View Record in Scopus](#)

[Nadeau et al., 1985](#)

P.H. Nadeau, M.J. Wilson, W.J. McHardy, J.M. Tait **The conversion of smectite to illite during diagenesis: evidence from some illitic clays from bentonites and sandstones**

Mineral. Mag., 49 (1985), pp. 393-400

[View Record in Scopus](#)

N. Nishiyama, T. Yokoyama **Does the reactive surface area of sandstone depend on water saturation?—The role of reactive-transport in water film**

Geochim. Cosmochim. Acta, 122 (2013), pp. 153-169

[ArticleDownload PDFView Record in Scopus](#)

[Nishiyama and Y](#)

C. Noiriel, L. Luquot, B. Madé, L. Rimbault, P. Gouze, J. van der Lee **Changes in reactive surface area during limestone dissolution: an experimental and modelling study**

Chem. Geol., 265 (2009), pp. 160-170

[ArticleDownload PDFView Record in Scopus](#)

[Noiriel et al., 200](#)

C. Noiriel, C.I. Steefel, L. Yang, J. Ajo-Franklin **Upscaling calcium carbonate precipitation rates from pore to continuum scale**

Chem. Geol., 318–319 (2012), pp. 60-74

[ArticleDownload PDFView Record in Scopus](#)

[Noiriel et al., 201](#)

D. Paganin, S.C. Mayo, T.E. Gureyev, P.R. Miller, S.W. Wilkins **Simultaneous phase and amplitude extraction from a single defocused image of a homogeneous object**

J. Microsc., 206 (2002), pp. 33-40

[CrossRefView Record in Scopus](#)

[Paganin et al., 2](#)

S.A. Parry, M.E. Hodson, S.J. Kemp, E.H. Oelkers **The surface area and reactivity of granitic soils: I. Dissolution rates of primary minerals as a function of depth and age deduced from field observations**

Geoderma, 237–238 (2015), pp. 21-35

[ArticleDownload PDFView Record in Scopus](#)

[Parry et al., 2015](#)

C.A. Peters **Accessibilities of reactive minerals in consolidated sedimentary rock: an imaging study of three sandstones**

Chem. Geol., 265 (2009), pp. 198-208

[ArticleDownload PDFView Record in Scopus](#)

[Peters, 2009](#)

V.T.H. Pham, P. Lu, P. Aagaard, C. Zhu, H. Hellevang **On the potential of CO<sub>2</sub>–water–rock interactions for CO<sub>2</sub> storage using a modified kinetic model**

Int. J. Greenh. Gas Con., 5 (2011), pp. 1002-1015

[ArticleDownload PDFView Record in Scopus](#)

[Pham et al., 201](#)

[Radlinski et al., 1](#)

A.P. Radlinski, C.J. Boreham, G.D. Wignall, J.S. Lin, *et al.* **Radlinski 1996 Microstructural evolution of source rocks during hydrocarbon generation A small angle scattering study**  
Phys Rev B, 53 (1996), pp. 14152-14160

[CrossRefView Record in Scopus](#)

[Rasband, 1997](#)

W.S. Rasband **ImageJ**  
Bethesda, Maryland, USA (1997)

F. Salehikhoo, L. Li **The role of magnesite spatial distribution patterns in determining dissolution rates: when do they matter?**

Geochim. Cosmochim. Acta, 155 (2015), pp. 107-121

[ArticleDownload PDFView Record in Scopus](#)

[Salehikhoo and Li](#)

A. Scislewski, P. Zuddas **Estimation of reactive mineral surface area during water-rock interaction using fluid chemical data**

Geochim. Cosmochim. Acta, 74 (2010), pp. 6996-7007

[ArticleDownload PDFView Record in Scopus](#)

[Scislewski and Zuddas](#)

C.I. Steefel, A.C. Lasaga **A coupled model for transport of multiple chemical-species and kinetic precipitation dissolution reactions with application to reactive flow in single-phase hydrothermal systems**

Am. J. Sci., 294 (1994), pp. 529-592

[CrossRefView Record in Scopus](#)

[Steefel and Lasaga](#)

C.I. Steefel, S. Carroll, P. Zhao, S. Roberts **Cesium migration in Hanford sediment: a multisite cation exchange model based on laboratory transport experiments**

J. Contam. Hydrol., 67 (2003), pp. 219-246

[ArticleDownload PDFView Record in Scopus](#)

[Steefel et al., 2003](#)

C.I. Steefel, C.A.J. Appelo, B. Arora, D. Jacques, T. Kalbacher, O. Kolditz, V. Lagneau, P.C. Lichtner, K.U. Mayer, J.C.L. Meeussen, S. Molins, D. Moulton, H. Shao, J. Šimůnek, N. Spycher, S.B. Yabusaki, G.T. YEH **Reactive transport codes for subsurface environmental simulation**

Comput. Geosci., 19 (2015), pp. 445-478

[CrossRefView Record in Scopus](#)

[Steefel et al., 2015](#)

C.I. Steefel, L.E. Beckingham, G. Landrot **Micro-continuum approaches for modeling pore-scale geochemical processes**

Rev. Mineral. Geochem., 80 (2015), pp. 217-246

[CrossRefView Record in Scopus](#)

[Steefel et al., 2015](#)

[Waldmann et al.](#)

S. Waldmann, A. Busch, K. van Ojik, R. Gaupp **Importance of mineral surface areas in Rotliegend sandstones for modeling CO<sub>2</sub>-water-rock interactions**

Chem. Geol., 378–379 (2014), pp. 89-109

[ArticleDownload PDFView Record in Scopus](#)

[Wang et al., 201](#)

H.-W. Wang, L.M. Anovitz, A. Burg, D.R. Cole, L.F. Allard, A.J. Jackson, A.G. Stack, G. Rothe **Multi-scale characterization of pore evolution in a combustion metamorphic complex, Hatrurim basin, Israel: combining (ultra) small-angle neutron scattering and image analysis**

Geochim. Cosmochim. Acta, 121 (2013), pp. 339-362

[ArticleDownload PDFView Record in Scopus](#)

[Weitkamp et al.](#)

Weitkamp, T., Haas, D., Wegrzynek, D., Rack, A., 2011. ANKAphase: software for single-distance phase retrieval from inline X-ray phase-contrast radiographs. urn:issn:0909-0495 18, 617–629.

[Zhu and Lu, 2013](#)

C. Zhu, P. Lu **The coupling of dissolution and precipitation reactions as the main contributor to the apparent field-lab rate discrepancy**

Proc. Earth Planet. Sci., 7 (2013), pp. 948-952

[ArticleDownload PDFView Record in Scopus](#)

[Zhu et al., 2006](#)

C. Zhu, D.R. Veblen, A.E. Blum, S.J. Chipera **Naturally weathered feldspar surfaces in the Navajo Sandstone aquifer, Black Mesa, Arizona: electron microscopic characterization**

Geochim. Cosmochim. Acta, 70 (2006), pp. 4600-4616

[ArticleDownload PDFView Record in Scopus](#)